Article

SOURCE DATA | TRANSPARENT PROCESS | OPEN ACCESS

THE EMBO JOURNAL

EZH2 inhibition stimulates repetitive element expression and viral mimicry in resting splenic B cells

Seung J Kim[1,2,3], Patti K Kiser[4], Samuel Asfaha[1,2,4,5], Rodney P DeKoter[6] & Frederick A Dick[1,2,4,*]

Abstract

Mammalian cells repress expression of repetitive genomic sequences by forming heterochromatin. However, the consequences of ectopic repeat expression remain unclear. Here we demonstrate that inhibitors of EZH2, the catalytic subunit of the Polycomb repressive complex 2 (PRC2), stimulate repeat misexpression and cell death in resting splenic B cells. B cells are uniquely sensitive to these agents because they exhibit high levels of histone H3 lysine 27 trimethylation (H3K27me3) and correspondingly low DNA methylation at repeat elements. We generated a pattern recognition receptor loss-of-function mouse model, called RIC, with mutations in *Rigi* (encoding for RIG-I), *Ifih1* (MDA5), and *Cgas*. In both wildtype and RIC mutant B cells, EZH2 inhibition caused loss of H3K27me3 at repetitive elements and upregulated their expression. However, NF-κB-dependent expression of inflammatory chemokines and subsequent cell death was suppressed by the RIC mutations. We further show that inhibition of EZH2 in cancer cells requires the same pattern recognition receptors to activate an interferon response. Together, the results reveal chemokine expression induced by EZH2 inhibitors in B cells as a novel inflammatory response to genomic repeat expression. Given the overlap of genes induced by EZH2 inhibitors and Epstein–Barr virus infection, this response can be described as a form of viral mimicry.

Keywords autoimmunity; heterochromatin; inflammation; therapeutic; virus
Subject Categories Chromatin, Transcription & Genomics; Immunology
DOI 10.15252/embj.2023114462 | Received 7 May 2023 | Revised 19 October 2023 | Accepted 25 October 2023 | Published online 7 November 2023
The EMBO Journal (2023) 42: e114462

Introduction

Enhancer of zeste homolog 2 (EZH2) is the catalytic subunit of the Polycomb Repressive Complex 2 (PRC2) that deposits di- and tri-methylation of histone 3 at lysine 27 (H3K27me2/3) (Cao *et al*, 2002; Kuzmichev *et al*, 2002; Margueron *et al*, 2008). These are repressive histone modifications that cooperate with histone 2a lysine 119 ubiquitination (H2AK119ub) to silence transcription and compact chromatin (Müller *et al*, 2002; Dellino *et al*, 2004; Francis *et al*, 2004; Wang *et al*, 2004; Ku *et al*, 2008; Eskeland *et al*, 2010; Leeb *et al*, 2010; Tamburri *et al*, 2020). The latter modification is catalyzed by the Polycomb Repressive Complex 1 (PRC1), and the two PRCs were originally described in *Drosophila* as repressors of homeotic genes that dictate segmentation along the anterior–posterior axis (Schuettengruber *et al*, 2007). In mammals, the catalytic activity of EZH2 in PRC2 facilitates roles in cell fate determination (Yin *et al*, 2015), stem cell renewal (Collinson *et al*, 2016), and tumorigenesis (Souroullas *et al*, 2016). For example, EZH2 is required for B cell differentiation in the bone marrow during hematopoiesis (Su *et al*, 2003), and germinal center (GC) formation (Béguelin *et al*, 2017). Furthermore, EZH2 overexpression and gain-of-function mutations have been identified in different cancer types and are prominent in B cell lymphomas (Varambally *et al*, 2002; Kleer *et al*, 2003; Velichutina *et al*, 2010; Wassef *et al*, 2015; Zhao *et al*, 2019; Béguelin *et al*, 2020). Mechanistically, somatic mutations at $EZH2^{Y641}$ render it dominantly active, increasing H3K27me3 globally, and repressing cell cycle control genes such as *CDKN2A* (Yap *et al*, 2011). This has prompted the development of EZH2 inhibitors that are either recently approved or are in clinical trials (McCabe *et al*, 2012; U.S. Food and Drug Administration, 2020; Morschhauser *et al*, 2020).

Regulation of gene expression represents only one facet of EZH2 activity. Repetitive sequences that make up the majority of mammalian genomes harbor H3K27me3 and other repressive epigenetic modifications (Kondo & Issa, 2003; Martens *et al*, 2005; Day *et al*, 2010; de Koning *et al*, 2011; Karimi *et al*, 2011; Bulut-Karslioglu *et al*, 2014; Liu *et al*, 2014; Ishak *et al*, 2016). These modifications repress transcription of repetitive elements and limit mobility in the host genome. Loss of epigenetic modifications such as H3K27me3 results in their upregulation. While a subset of

1 London Regional Cancer Program, Children's Health Research Institute, London, ON, Canada
2 London Health Sciences Research Institute, London, ON, Canada
3 Department of Biochemistry, Western University, London, ON, Canada
4 Department of Pathology and Laboratory Medicine, Western University, London, ON, Canada
5 Department of Medicine, Western University, London, ON, Canada
6 Department of Microbiology & Immunology, Western University, London, ON, Canada
*Corresponding author. Tel: +1 519 685 8500 x 53027; Fax: +1 519 685 8616; E-mail: fdick@uwo.ca

genomic repeats have been exapted to serve the host cell, their derepression and subsequent upregulation have been linked to tumorigenesis (Howard *et al*, 2008; Lamprecht *et al*, 2010; Levin & Moran, 2011; Lock *et al*, 2014; Doucet-O'Hare *et al*, 2015; Ewing *et al*, 2015; Babaian & Mager, 2016; Desai *et al*, 2017; Rodriguez-Martin *et al*, 2020). Overall, the impact of EZH2 in mediating repression of repetitive elements in normal mammalian physiology is relatively unexplored.

Pharmacologically induced upregulation of repetitive elements by inhibiting repressive epigenetic writers has been shown to elicit anti-tumor responses (Chiappinelli *et al*, 2015; Roulois *et al*, 2015; Liu *et al*, 2018; Morel *et al*, 2021). Tumor cells treated with small molecule inhibitors against DNA and histone methyltransferases derepress the transcription of repetitive elements (Chiappinelli *et al*, 2015; Roulois *et al*, 2015; Liu *et al*, 2018; Morel *et al*, 2021). These transcripts form secondary structures that are detected by nucleic-acid sensing pattern recognition receptors (PRRs) such as RIG-I, MDA5, and cGAS. In general, PRRs are a part of the innate immune surveillance that detect molecular patterns associated with infectious agents such as bacteria and viruses, and signals downstream to either neutralize the threat or further activate the adaptive immune system (Schmidt *et al*, 2012; Goubau *et al*, 2013). This phenomenon has been described as 'viral mimicry', as upregulation of repetitive elements and activation of PRRs mimics a viral infection. While viral mimicry has been demonstrated in cancer cells as a therapeutic paradigm, it is unclear if untransformed cells with normal establishment of DNA and histone methylation to silence repeat expression are susceptible to viral mimicry responses caused by therapeutic agents.

Interestingly, mice with defective EZH2 recruitment to repetitive elements caused by a mutation in the retinoblastoma tumor suppressor protein (pRB) ectopically express repeats and succumb to lymphomas that often arise in the spleen and lymph nodes (Ishak *et al*, 2016). To investigate the significance of EZH2 regulation of genomic repeats, we utilized pharmacological inhibition of EZH2 to investigate its acute effects on repeat regulation. Short-term EZH2 inhibition with three different inhibitors induced expression of repetitive elements specifically in B cells and was accompanied by inflammation and cell death. To investigate if this effect is dependent on repeat expression, we generated triple mutant *Rigi*, *Ifih1* (MDA5), and *Cgas* mutant mice (referred to as RIC mutant) to block detection by pattern recognition receptors. In both WT and RIC mutant B cells, EZH2 inhibition induced loss of H3K27me3 at repetitive elements and increased repeat expression. Unlike WT, the RIC mutant mice failed to upregulate pro-inflammatory chemokine genes and recruit effector immune cells, preserving B cell viability. In contrast, treatment of murine cancer cells with the same EZH2 inhibitor activates a PRR-dependent interferon response. This dichotomy of gene expression programs emphasizes that normal, resting B cells are capable of a unique form of viral mimicry.

Results

Pharmacological EZH2 inhibition causes splenic B cell apoptosis

Constitutive loss of EZH2-mediated repression of repetitive elements in immune cells caused by mutations in *Rb1* leads to their sporadic expression and the eventual formation of lymphomas (Ishak *et al*, 2016). To determine the effect of acute inhibition of EZH2 in resting splenocytes, 6–8 week-old-mice were injected with vehicle or three different EZH2 inhibitors (GSK343, UNC1999, and EPZ6438). Spleens were harvested for histology and flow cytometry 1 or 2 days later (Fig 1A). In contrast to vehicle treatment, tingible body macrophages were evident within follicles upon treatment with all three EZH2 inhibitors, suggesting B cell death and engulfment (Fig 1B and C). Distinct staining for cleaved caspase 3 in spleen follicles (Fig 1B), the increased percentage of positively stained cells in the spleen (Fig 1D), and reduction in B cells (Fig 1E) further suggests B cell death in response to EZH2 inhibition. Following 5 days of GSK343 treatment we performed H&E staining as well as IHC staining for CD68, a marker of monocytes and macrophages. This revealed that GSK343 treatment extensively reduced follicular regions of spleens and the smaller follicles that remained included notable acellular regions (Appendix Fig S1A). CD68 staining in vehicle treated controls was largely restricted to red pulp while GSK343 induced infiltration of these cells into the follicles (Appendix Fig S1B). Overall, these results show that targeted, short-term inhibition of EZH2 extensively disrupts splenic follicles. EZH2 inhibition causes apoptotic B cell death and the coincident arrival of tingible body macrophages indicates it is associated with inflammation. This was observed with three chemically distinct inhibitors, emphasizing that acute EZH2 inhibition underlies these observations.

Unique B cell heterochromatin structure allows EZH2 inhibition to increase repeat expression

Given EZH2's role in B cell lineage development (Su *et al*, 2003), we sought to understand how its inhibition affects transcript levels in resting B cells and compare it with other resident cells of the spleen. Since EZH2 inhibition causes apoptosis *in vivo* (Fig 1B), we treated splenic B cells *in vitro* with GSK343 and harvested before loss of viability was observed to determine the most direct impact of these inhibitors.

We separated erythrocyte-lysed splenocytes into a $CD43^-$ mature splenic B cell fraction and a $CD43^+$ fraction composed of neutrophils, T cells, and others using paramagnetic beads (Figs 2A and EV1A). We treated B cell cultures with DMSO or 1 μM GSK343 for 48 h in biological triplicates. RNA was extracted and sequenced followed by analysis with two established analysis pipelines (Criscione *et al*, 2014; Liao *et al*, 2014; Teissandier *et al*, 2019) to quantify expression of repetitive elements annotated in RepeatMasker (Karolchik *et al*, 2004). This experiment revealed that B cells upregulated numerous repetitive elements including LINE/SINEs, LTR containing ERVs, satellite sequences, and DNA transposons (Figs 2B and EV1B). To confirm these findings with multiple EZH2 inhibitors and compare with other cells in the spleen, we carried out qRT–PCR for three classes of repeats identified as increased by RNA-seq. Figure 2C shows significant upregulation of three different classes of repetitive elements upon EZH2 inhibitor treatment of B cells (top row), but these elements were infrequently altered by the same treatment of $CD43^+$ splenocytes (bottom row). These data indicate repeat misexpression is a unique consequence of EZH2 inhibition in B cells and not other resident splenocytes.

To understand the regulation of B cell heterochromatin better, cultures of B and $CD43^+$ cells were incubated for 48 h with

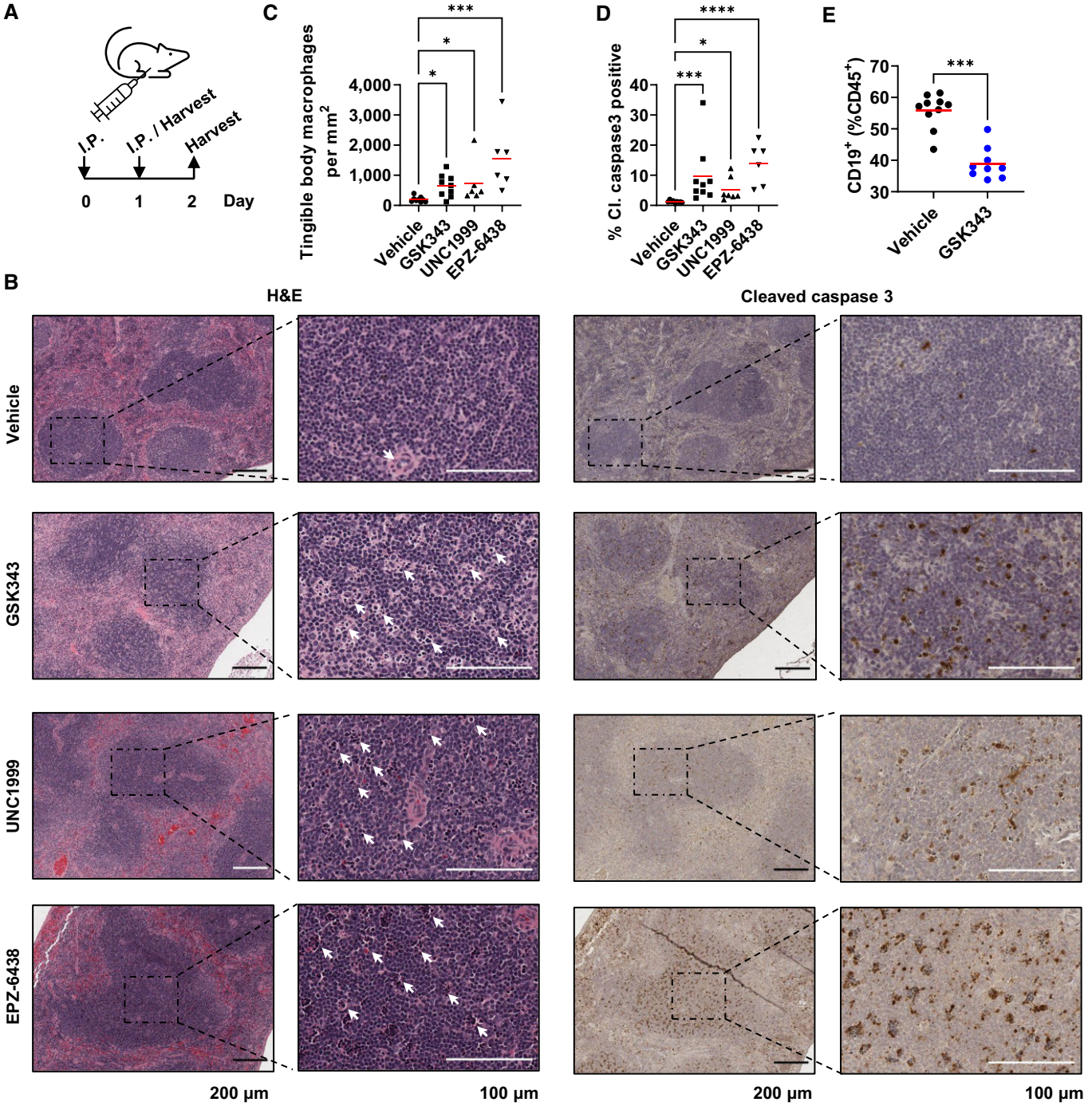

Figure 1. EZH2 inhibition induces B cell apoptosis and inflammation.

A Schematic illustrating I.P. drug injection schedule for 1 or 2-day treatments.

B H&E staining of spleens following 2 days of vehicle, 100 mg/kg GSK343, 100 mg/kg UNC1999, or 1 day of 100 mg/kg EPZ6438. White arrows indicate tingible body macrophages (left). DAB staining for cleaved caspase 3 on consecutive spleen sections corresponding to H&E staining. Scale bars: 200 µm (wide), 100 µm (zoom).

C Number of tingible body macrophages per mm^2 in the spleens from vehicle or EZH2 inhibitor treated mice (n = 6–9 biological replicates). Horizontal line indicates the mean. *P < 0.05, ***P < 0.001 by one-way ANOVA with Dunn's multiple test correction.

D Percentage of cells positive for cleaved caspase 3 in the spleens from vehicle or EZH2 inhibitor treated mice (n = 6–9 biological replicates). *P < 0.05, ***P < 0.005, ****P < 0.0005 by one-way ANOVA with Kruskal–Wallis multiple test correction.

E Percentage of $CD19^+$ cells from spleens of vehicle or EZH2 inhibitor treated mice (n = 9–10 biological replicates). ***P < 0.05, by unpaired Student's t-test.

Source data are available online for this figure.

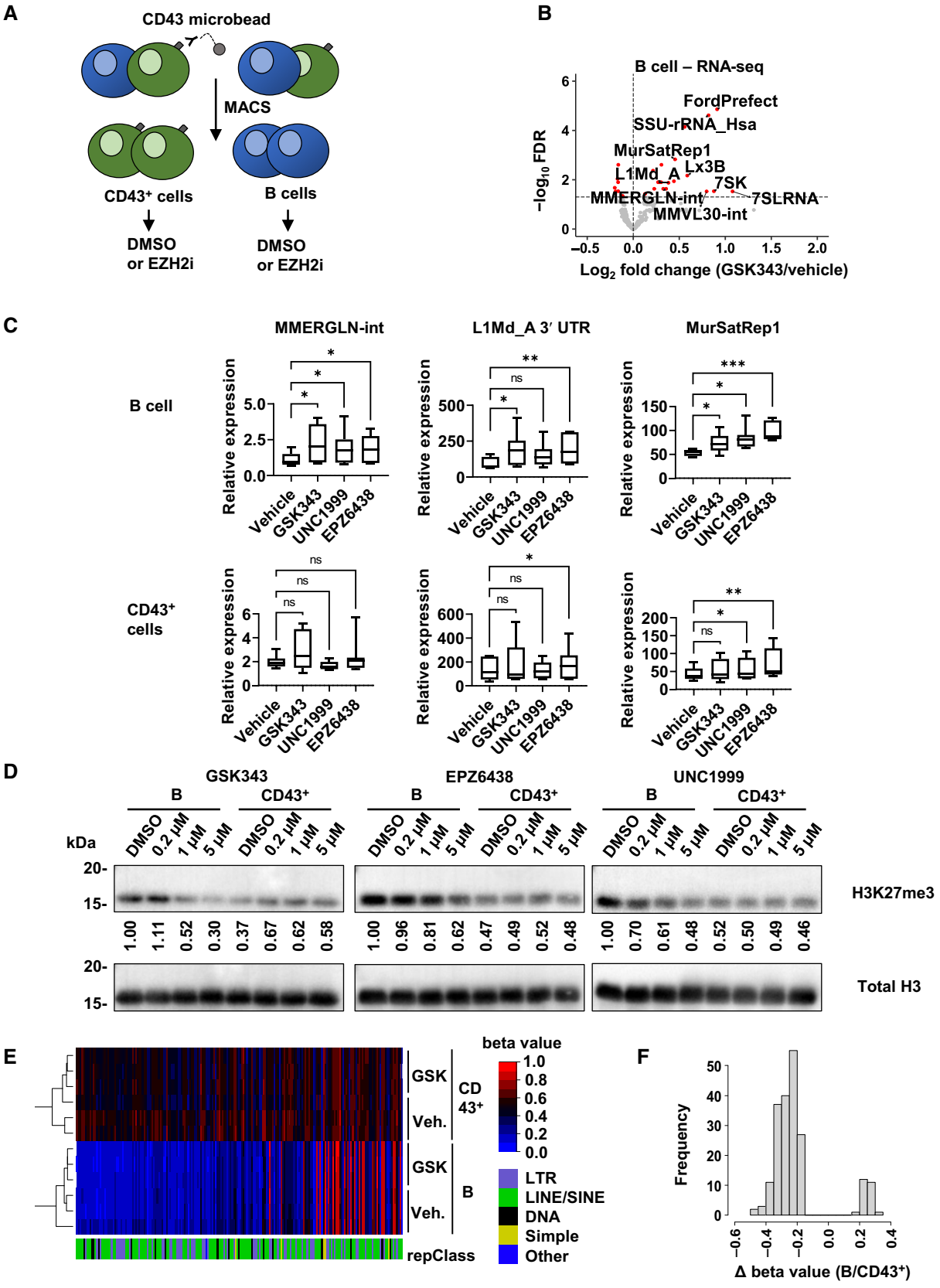

Figure 2.

Figure 2. Splenic B cells are uniquely sensitive to EZH2 inhibitors.

A Schematic describing magnetic-assisted cell sorting (MACS) to separate B and CD43$^+$ cells from the spleen.

B Volcano plot depicting up- or downregulated repetitive elements in purified splenic B cells treated with DMSO or 1 μM GSK343 for 48 h in culture (n = 3 biological replicates).

C qRT–PCR of indicated repetitive elements in splenic B cells (top row) or CD43$^+$ cells (bottom row) treated with DMSO, GSK343, UNC1999 or EPZ6438 (n = 7 biological replicates). Whiskers represent the 10th and the 90th percentile. Boxes represent the first quartile, the median, and the third quartile. *P < 0.05, **P < 0.005, ***P < 0.001 by one-way ANOVA with Dunn's multiple test correction.

D Western blots of H3K27me3 and total H3 from histone extracts of B or CD43$^+$ cells treated with DMSO or increasing concentrations of indicated EZH2 inhibitors for 48 h in culture. Numbers below H3K27me3 blots refer to H3K27me3 signal normalized to total H3.

E Heatmap of DNA methylation probe beta values at top 200 differentially methylated probes annotated with repetitive elements by repClass between DMSO-treated B and CD43$^+$ cells.

F Histogram of difference in beta values (DMSO-treated B vs. CD43$^+$ cells) among top 200 differentially methylated probes shown in (E).

Source data are available online for this figure.

increasing concentrations of EZH2 inhibitors (Fig 2D). Histones were extracted and analyzed by Western blotting for H3K27me3 to directly investigate the effect of EZH2 inhibition. This demonstrated that B cells have higher baseline H3K27me3 compared to CD43$^+$ cells (Fig 2D). In addition, loss of H3K27me3 was observed with increasing inhibitor concentration in B cells with all three EZH2 inhibitors (Fig 2D). Cells in the CD43$^+$ fraction did not show an obvious reduction in H3K27me3 levels in response to any of these treatment conditions. This indicates a unique reliance on EZH2 for the maintenance of heterochromatin in B cells that is distinct from other cell types in the spleen.

Repression of repeat expression is also known to be mediated by DNA methylation; therefore, we also investigated its status in B and CD43$^+$ cells. We performed a genome-wide DNA methylation microarray on DNA extracted from vehicle or GSK343 treated B and CD43$^+$ cells. Differential beta value analysis between vehicle treated B vs. CD43$^+$ cells revealed that probes annotated as representing repetitive elements had low levels of DNA methylation in B cells compared to CD43$^+$ splenocytes (Fig 2E). As expected, GSK343 treatment did not affect DNA methylation in either cell fraction. Only a small proportion of differentially methylated repeat probes was more methylated in B cells compared to the CD43$^+$ fraction (Fig 2F). By comparison, DNA methylation levels observed at probes annotated for promoters, genes or CpG islands displayed much greater similarity between B and CD43$^+$ populations (Fig EV1C). These data demonstrate low level DNA methylation at repeat elements uniquely in B cells. Taken together, these experiments show that splenic B cells specifically upregulate transcription of repetitive elements upon EZH2 inhibition. This corresponds with loss of H3K27me3 and constitutively low levels of DNA methylation at repetitive elements.

Pattern recognition receptors are required for EZH2 inhibitor-induced B cell death in the spleen

Ectopic expression of repetitive elements and subsequent inflammatory signaling are described as a state of viral mimicry (Ishak & De Carvalho, 2020; Chen *et al*, 2021). Transcripts from repetitive elements form secondary structures that mimic those of viral replication and transcription. Cytosolic nucleic acid sensing pattern recognition receptors (PRRs) such as RIG-I, MDA5 and cGAS bind to dsRNA/DNA to activate a signaling cascade that upregulates inflammatory gene expression. Notably, others have shown that these cytosolic PRRs are mechanistically required for DNMT or EZH2 inhibition-induced anti-tumor immune responses. We sought to determine if activation of pattern recognition receptors in splenic B cells underpins the inflammatory response and cell death following EZH2 inhibition.

We created a loss of function mouse model in which PRR genes are disrupted. Briefly, three gRNAs, each targeting a coding exon for one of *Rigi*, *Ifih1* (MDA5), and *Cgas* were microinjected with a Cas9 expressing mRNA into single-cell zygotes to simultaneously mutate all three genes (Wang *et al*, 2013) (Fig 3A). The resulting founder pups were bred together to create biallelic F1 mice that

Figure 3. *Rigi/Ifih1/Cgas* (RIC) triple mutant mice are resistant to EZH2 inhibitor killing of B cells.

A Schematic highlighting the key steps of generating RIC triple mutant mice. gRNAs and Cas9 mRNA are microinjected into zygotes and transplanted into a surrogate female. Resulting mosaic founders are bred together to generate biallelic triple mutant mice.

B Western blots of RIG-I and cGAS from whole cell extracts of WT and RIC mutant splenocytes.

C Western blots of MDA5 from whole cell extracts of WT and RIC mutant splenocytes harvested from mice injected with poly(I:C).

D Western blots of cGAS pulldown with biotinylated ISD45 probe and streptavidin beads from whole cell extracts of WT and RIC mutant splenocytes.

E H&E staining of the spleens following 2 days of vehicle or 100 mg/kg GSK343 in WT or RIC mutant mice. White arrows indicate tingible body macrophages. Scale bars: 100 μm.

F Percentage of cells positive for cleaved caspase 3 in the spleens from vehicle or GSK343 I.P. injected RIC mutant mice (n = 6–9 biological replicates). Horizontal line indicates the mean. ns P > 0.05 by Mann–Whitney test.

G Dose response curves of WT and RIC mutant splenic B cells to GSK343. Viability was quantified by trypan blue exclusion assay (n = 3 biological replicates). Error bars represent the standard deviation.

H Schematic describing adoptive transfer of CD45.1 WT B cells into CD45.2 RIC mutant mice, followed by vehicle or GSK343 injections.

I Percentage of CD45.1$^+$ CD19$^+$ adoptively transferred, WT B cells in RIC mutant spleens upon vehicle or GSK343 injections (n = 3 biological replicates). *P < 0.05 by unpaired Student's t-test.

Source data are available online for this figure.

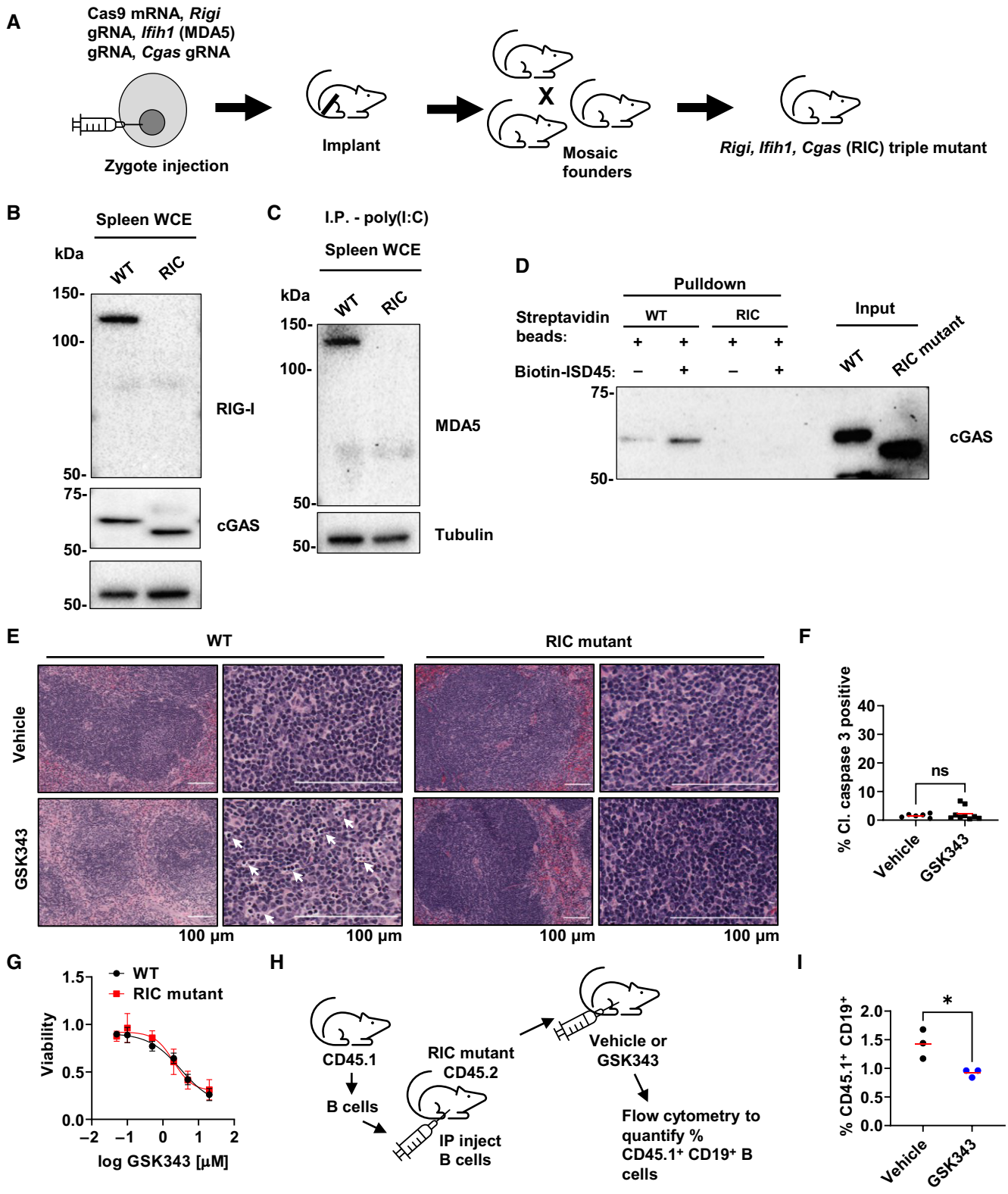

Figure 3.

were characterized for their mutant alleles (Fig EV2A). Mutants were identified using a restriction fragment length polymorphism assay to identify indels in the three genes in F1 mice (Fig EV2B and C). All mutant alleles in our triple mutant colony were sequenced to characterize how they disrupt their respective gene (Appendix Table S1). Lastly, we sought to identify any off-target

mutations created by the gRNAs in the F1 mice that we bred for experiments. We sequenced the two highest ranked coding and non-coding, *in silico* predicted (Cradick *et al*, 2014), off-target loci per gRNA (six in total) in the three F1 mice. Out of 36 possible alleles, we only found two, one-bp deletions and both were in non-coding regions (Appendix Table S2) confirming high fidelity of targeting by this strategy. All triple mutant *Rigi*, *Ifih1*, and *Cgas* mice (henceforth called RIC mutant) used in this study are descendants from these three F1 animals and were compared against C57BL/6NCrl controls.

We characterized expression from these mutant alleles by Western blotting. RIC mutant splenocytes completely lost RIG-I and MDA5 expression (Fig 3B and C), confirming that *Rigi* and *Ifih1* mutations are null alleles. The truncated cGAS detected by Western blotting (Fig 3B) agrees with the 48-bp deletions found in two distinct *Cgas* alleles (Fig EV2D and E). These N-terminal, in frame deletions, encode functionally inactive cGAS as it fails to bind a known dsDNA target, ISD45, in a streptavidin-biotin pull-down assay (Hansen *et al*, 2014) (Fig 3D). Furthermore, streptavidin alone has been shown to bind and activate cGAS, and truncated cGAS has also lost this interaction (Zhang *et al*, 2020) (Fig 3D).

To understand the role of PRRs in the response to EZH2 inhibition, systemic treatment of RIC mutant mice with GSK343 was performed and spleens were examined after 2 days. Infiltration of tingible body macrophages was less prominent in RIC mutant follicles (Fig 3E). Furthermore, the percentage of cells positive for cleaved caspase 3 was not significantly increased upon GSK343 treatment in RIC mutants (Fig 3F). These observations suggest that the functional loss of the cytosolic PRRs in the RIC mutant largely abrogates the cell death phenotype in spleens of GSK343 treated mice. Furthermore, WT or RIC mutant B cells were isolated from spleens and treated with GSK343. This revealed a similar dose response to GSK343 (Fig 3G), indicating that the cell intrinsic response to GSK343 is unaffected by the RIC mutations. However, all cells in the RIC mutant mouse are disrupted for PRRs and not just their B cells. PRR mutations may affect other cell functions, possibly those involved in an inflammatory response that could prevent B cell death in response to EZH2 inhibitors. To rule out this possibility we isolated B cells from C57BL/6 CD45.1 donors and transferred them to CD45.2 RIC mutant recipients where they were treated with GSK343 for 2 days (Fig 3H). Flow cytometry to identify CD45.1 B cells from the spleens of these mice revealed that GSK343 treatment diminished WT B cells in a RIC mutant host (Fig 3I). These data argue that the mutant host has no ability to block B cell death induced by inflammation from EZH2 inhibitors. Collectively, triple mutant RIC mice that are deficient for PRR function demonstrate that PRRs respond to misexpressed repeats in B cells following EZH2 inhibitor treatment, causing inflammation and cell death.

EZH2 inhibition induces H3K27me3 loss at repetitive elements in B cells

We investigated the effect of EZH2 inhibition at the chromatin level in isolated WT and RIC mutant B cells. We performed ChIP-seq for H3K27me3 in DMSO or GSK343 treated cells in biological duplicates. We obtained high-quality sequencing libraries from input controls and H3K27me3 associated fragments (Fig EV3A–C), we then identified H3K27me3 peaks using MACS2 and quantified read fragment enrichment at those peaks. As expected, most high-scoring peaks found in vehicle treated samples were shared by WT and RIC mutants (Fig EV3D), confirming that the baseline locations of H3K27me3 deposition is independent of PRRs. We then compared loss of H3K27me3 upon GSK343 treatment with their respective vehicle treated genotype controls. Figure 4A depicts normalized read fragment enrichment where each row represents a scaled peak length with 1 kb flanking each end. The sum of the rows represents all the peaks identified in vehicle-treated, control ChIP samples for each genotype (WT and RIC mutant). At these baseline H3K27me3 peaks, GSK343 decreased enrichment in both WT and RIC mutants (5^{th} and 6^{th} vs. 7^{th} and 8^{th} columns). Next, we sought to determine which genomic features were associated with these H3K27me3 peaks. We annotated the peaks found in each ChIP sample (pooling biological replicates together) based on their proximity to known genes. The absolute fold decrease in peak count was the greatest in intronic and intergenic regions for both WT and RIC mutant upon GSK343 treatment (Fig 4B and C). Intronic and intergenic regions contain repetitive elements and the absolute number of repetitive elements that intersect with peaks was similarly decreased upon GSK343 treatment in both genotypes (Figs 4D and E, EV3E and F). In addition, we confirmed that H3K27me3 enrichment at peaks intersected with specific repeat element families identified by RNA-seq and that these were decreased upon GSK343 treatment in both genotypes (Fig 4F). These ChIP experiments show that EZH2 inhibition decreases H3K27me3 preferentially at repetitive elements in both WT and RIC mutant B cells. It confirms that inactivation of cytosolic PRRs has no bearing on H3K27me3 containing heterochromatin or the effect of EZH2 inhibition on H3K27me3 reduction.

Figure 4. GSK343 induces loss of H3K27me3 at repetitive elements in splenic B cells.

A Heatmap of input and H3K27me3 ChIP-seq read enrichment at all peaks called in DMSO-treated samples. Splenic B cells were treated with either DMSO or 1 μM GSK343 for 48 h (n = 2 biological replicates). Enrichment was quantified as reads per genomic content (RPGC). Each row represents a scaled DMSO peak location with 1 kb flanking each end. Rows are sorted by decreasing enrichment.

B Distribution of peaks among the indicated genomic features in each sample.

C Fold-change of the number of called peaks annotated with indicated genomic features. Horizontal dotted lines indicate the average overall fold change.

D Number of repetitive elements in each indicated repClass that intersect with called peaks in each sample condition shown.

E Enrichment profiles of H3K27me3 ChIP-seq reads at peaks called in DMSO or GSK343 treated samples intersecting with repetitive elements. Each box shows the average profile of scaled repetitive elements with 1 kb flanking each end. Biological duplicates for each treatment condition are shown as separate curves.

F Three genome track views showing normalized coverage (RPGC) of H3K27me3 signal track for indicated sample conditions at repetitive elements. Horizontal bars indicate either peak calls or repetitive element annotations.

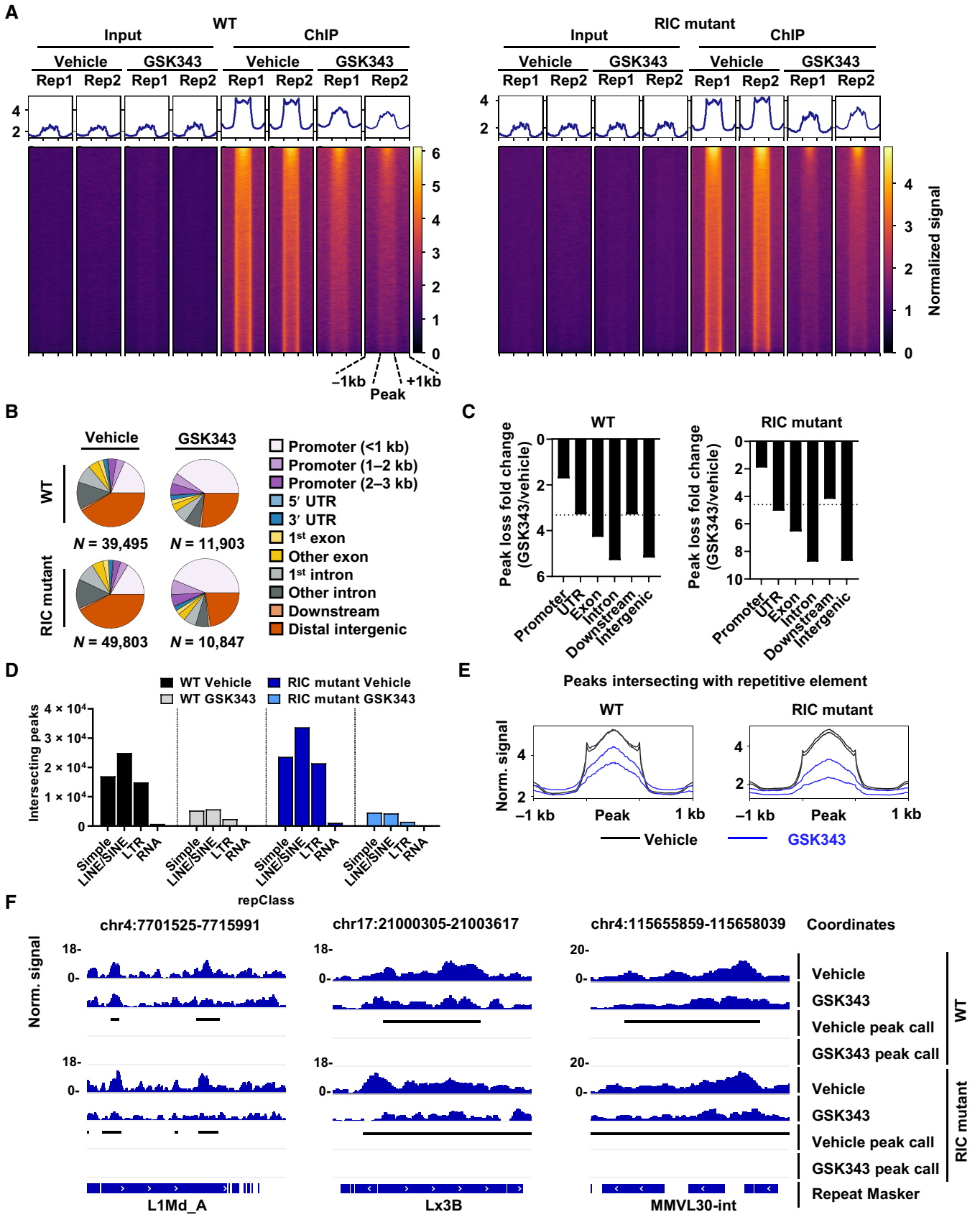

Figure 4.

Cytosolic PRRs are required for pro-inflammatory gene expression upon EZH2 inhibition

Since GSK343 induces comparable loss of H3K27me3 in both WT and RIC mutant B cells, we next investigated its effects on the transcriptome. WT and RIC mutant B cells were treated with DMSO or GSK343 as before, RNA was extracted, and we performed RNA-seq to identify differentially expressed repetitive elements, genes, and significantly enriched gene sets.

This revealed that the most differentially upregulated genes upon EZH2 inhibition were correlated with loss of H3K27me3 at their promoters (Fig 5A), and this effect was observed in both genotypes. Consistent with similar effects by GSK343 on H3K27me3 between WT and RIC mutant mice, upregulation of many of the same repeats also took place in RIC mutants (Figs 5B and EV4A and B). From these analyses, we conclude that EZH2 inhibition leading to H3K27me3 loss causes similar increases in gene and repeat transcript levels in WT and RIC mutants.

To understand the consequences of PRR loss in response to EZH2 inhibition, we searched for differences in gene expression that were not the consequence of direct regulation by H3K27me3. Most genes that were significantly up or downregulated in GSK343 treated RIC mutant cells showed a similar change in WT (Fig EV4C), and many gene sets were commonly upregulated in both WT and RIC mutants (Figs 5C and EV4D, Tables EV1–EV4, and Datasets EV1 and EV2). However, RIC mutants showed a smaller absolute number of genes with altered expression compared to WT (Fig EV4C). Furthermore, several pathways that were significantly enriched in WT, were missing in RIC mutants (Fig 5C). In particular, pathways related to chemotaxis were enriched in GSK343 treated WT samples but not RIC mutants, suggesting a potential source of inflammatory signaling dependent on PRRs. We note that interferon signaling, described in previous studies of viral mimicry upon epigenetic inhibition (Chiappinelli *et al*, 2015; Roulois *et al*, 2015; Liu *et al*, 2018; Morel *et al*, 2021), is not activated by GSK343 in B cells (Fig 5C and D). Upregulation of monocyte chemotaxis genes was more consistent and robust in WT compared to RIC mutants (Fig 5E). Notably, several of these genes were secreted chemokines with pro-inflammatory functions. Importantly, upregulation of these chemokines in WT, but not RIC mutant B cells, was not associated with direct loss of H3K27me3 as evidenced by the absence of peaks at these genes under all experimental conditions (Fig 5F). This suggests that their upregulation is mediated by GSK343-induced repetitive element expression, activation of cytosolic PRRs and subsequent signaling. Consistent with gene expression data, detection of secreted cytokines by array analysis demonstrates RIC dependent upregulation of MIP-1α (encoded by *Ccl3*) and MDC (encoded by *Ccl22*) (Fig 5G). In sum, these data indicate that the cytosolic PRRs are required to upregulate chemokine production upon EZH2 inhibition with GSK343 and this effect is blocked in RIC mutants.

EZH2 inhibition induces an NFκB dependent gene expression program that resembles B cell infection by Epstein–Barr virus

To understand if EZH2 inhibition induced inflammation and B cell death represent synthetic chemical effects or are triggering a natural physiological response, we compared our findings with B cells following an *in vitro* viral infection. We performed the same GSEA on existing RNA-seq data of Epstein–Barr Virus (EBV) infected human B cells (Wang *et al*, 2019a, Data ref: Wang *et al*, 2019b). This revealed that monocyte chemotaxis was a commonly shared and highly ranked gene expression category from both EBV infection and EZH2 inhibition (Fig 6A and B). In contrast, IFN-related gene sets were not significantly upregulated (Fig EV4E). Furthermore, we found that the monocyte chemotaxis gene set was significantly enriched in EBV-infected cells compared to control at five out of six time points following infection (Fig 6C). Next, we compared the number of gene sets that were commonly upregulated between EBV-infected human B cells and GSK343 treated WT or RIC mutant B cells. This revealed that gene sets upregulated in RIC mutant B cells were generally exclusive to themselves (red), As expected, human B cells infected with EBV for various durations shared many commonly upregulated gene sets. Importantly, GSK343 treated WT B cells shared more gene sets with EBV-infected B cells (purple) compared to RIC mutants (yellow). Taken together, these data suggest that loss of PRRs in RIC mutants abrogated upregulation of gene sets that are induced in a bona fide viral infection in human B cells. Based on this similarity we describe EZH2 inhibition as a viral mimicry response and emphasize that its mechanism of action is clearly distinct from previously reported viral mimicry that is highly dependent on interferon signaling.

Figure 5. Cytosolic PRRs are required for GSK343-induced inflammatory signaling in B cells.

A Scatter plot showing a negative correlation between loss of H3K27me3 near promoters and upregulation of nearby genes in WT and RIC mutant splenic B cells. Top 50 upregulated genes annotated with H3K27me3 fold change nearby are shown. Fold change reflects GSK343 treatment compared to vehicle. A test for non-parametric Spearman's correlation was performed.

B Volcano plot depicting up- or downregulated repetitive elements in RIC mutant splenic B cells treated with DMSO or 1 μM GSK343 for 48 h in culture ($n = 3$ biological replicates).

C Bar plot depicting adjusted *P* values (FWER) of GSEA of Gene Ontology (GO) biological processes and Hallmark gene sets based on a weighted Kolmogorov–Smirnov statistic. Horizontal dotted line indicates *P* value cut-off at 0.1.

D Net enrichment scores (NES), *q*-value (FWER) and rank among gene sets (color legend) for chemotaxis or IFN-related gene sets for WT (left) and RIC mutant (right) based on a weighted Kolmogorov–Smirnov statistic. Horizontal dotted line indicates *P* value cut-off at 0.1.

E Expression heatmap of genes annotated in "monocyte chemotaxis" gene set in WT and RIC mutant splenic B cells. Expression is shown as a *Z*-score of the mean of each row and chemokine genes are indicated. FDR cutoff: 0.05.

F Genome track view showing normalized coverage (RPGC) of H3K27me3 signal tracks at genes encoding chemokines in "monocyte chemotaxis" GO pathway.

G Quantification of MIP-1α (*Ccl3*) and MDC (*Ccl22*) from cell culture supernatant of WT and RIC mutant splenic B cells treated with DMSO or 1 μM GSK343 for 48 h in culture ($n = 3$ biological replicates). $^{*}P < 0.05$, $^{**}P < 0.001$ by two-way ANOVA with Dunnett's multiple test correction.

Source data are available online for this figure.

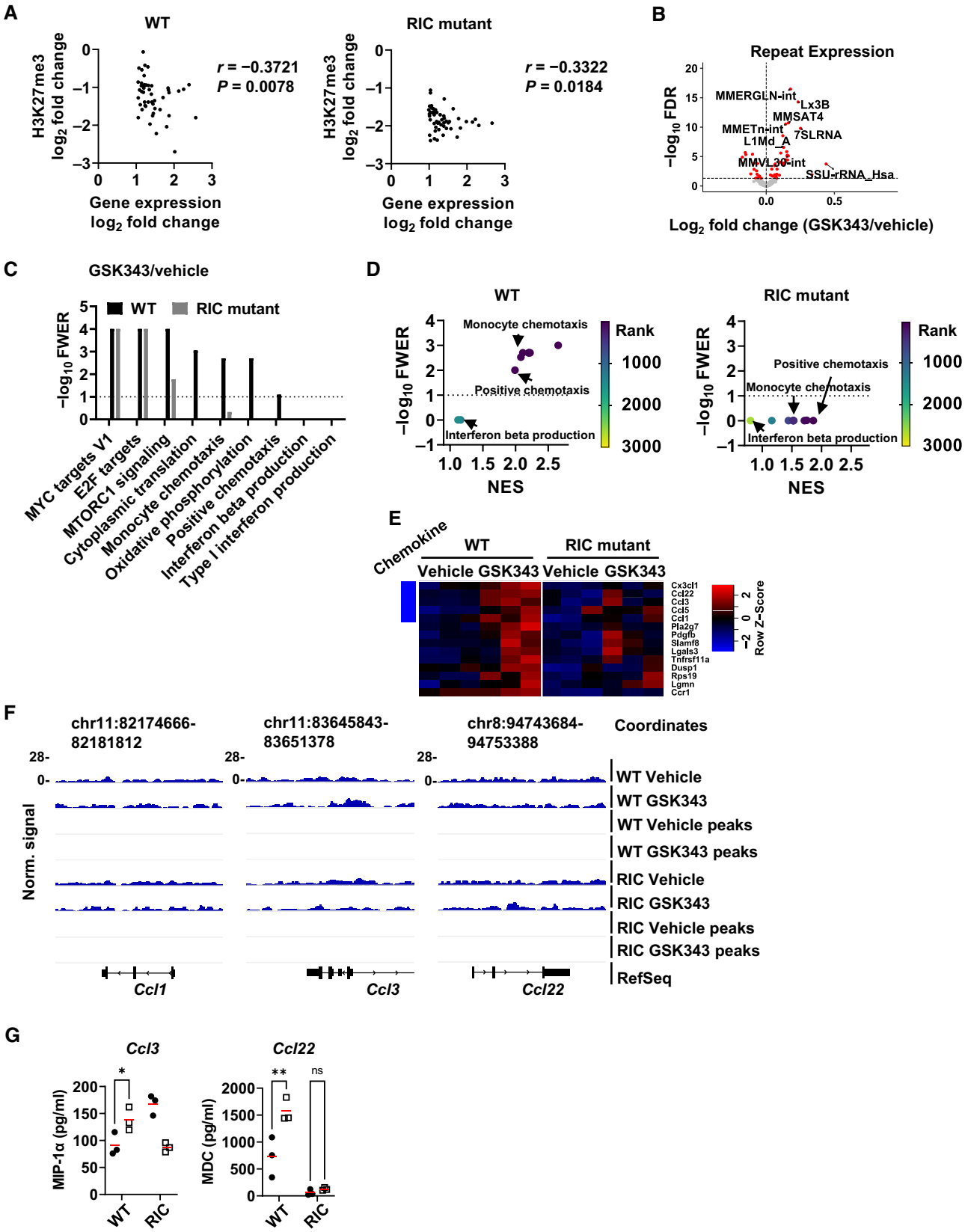

Figure 5.

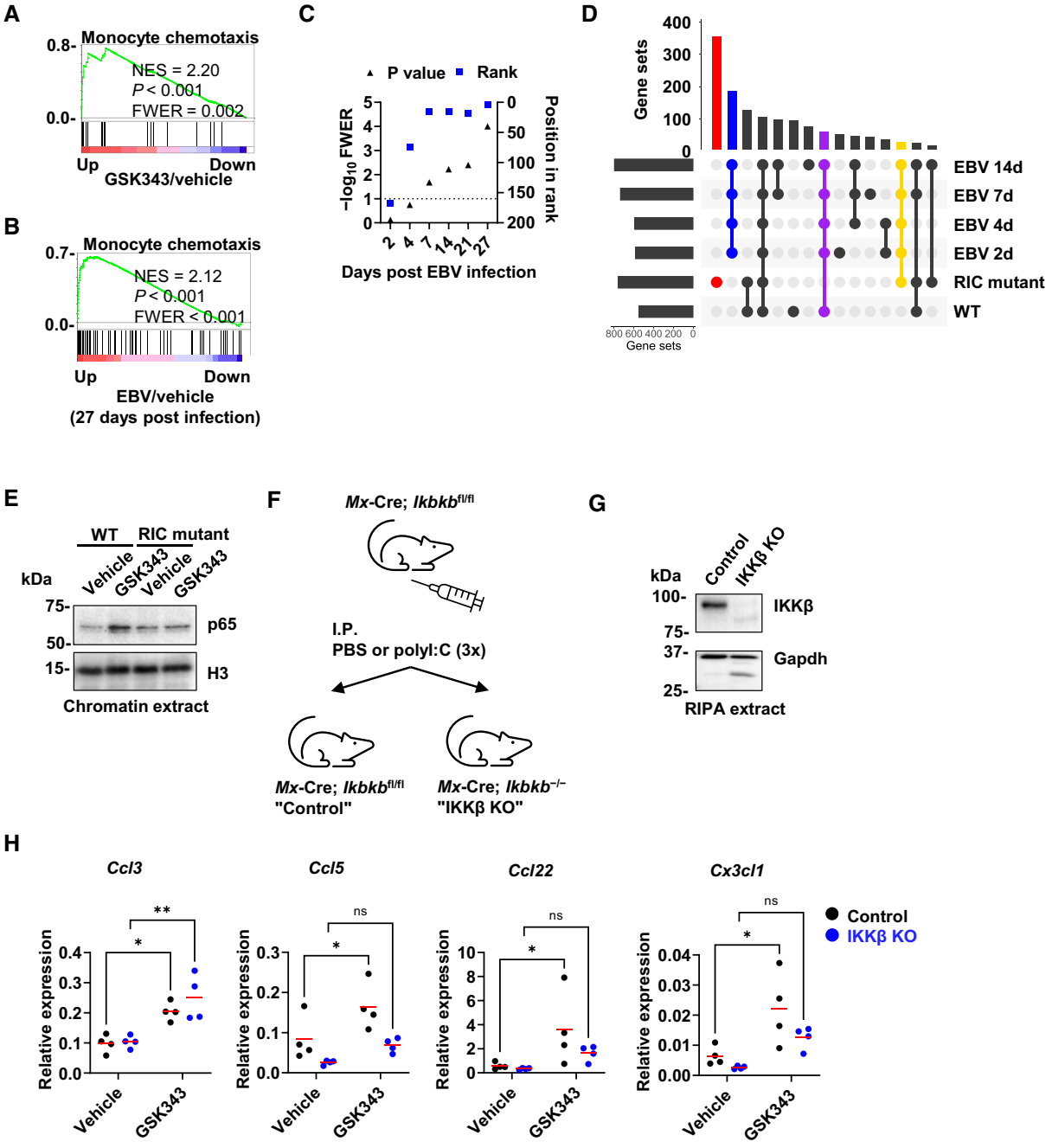

Figure 6. EZH2 inhibition mimics B cell infection by Epstein–Barr Virus.

A GSEA plot of "monocyte chemotaxis" GO gene set significantly enriched in GSK343-treated splenic B cells compared to vehicle based on a weighted Kolmogorov–Smirnov statistic.

B GSEA plot of "monocyte chemotaxis" GO gene set significantly enriched in EBV-infected human B cells compared to control based on a weighted Kolmogorov–Smirnov statistic.

C Adjusted *P* values (FWER) and position in ranked list (out of all tested gene sets) of "monocyte chemotaxis" GO biological process pathway at indicated days post EBV infection in human B cells based on a weighted Kolmogorov–Smirnov statistic. Horizontal dotted line indicates *P* value cut-off at 0.1.

D Upset plot showing numbers of commonly or exclusively upregulated GO biological process gene sets upon EBV infection or GSK343 treatment.

E Western blot of NFκB p65 in chromatin fractions from WT and RIC mutant splenic B cells treated with DMSO or 1 μM GSK343 for 48 h in culture. Representative image of biological duplicate experiments.

F Schematic describing the strategy to genetically delete IKKβ.

G Western blot showing IKKβ expression in control or KO splenic whole cell extracts.

H qRT–PCR quantification of indicated chemokines in splenic B cells treated with DMSO or GSK343 ($n = 4$ biological replicates). ns $P > 0.05$, *$P < 0.05$, **$P < 0.005$ by two-way ANOVA with Sidak's multiple test correction.

Source data are available online for this figure.

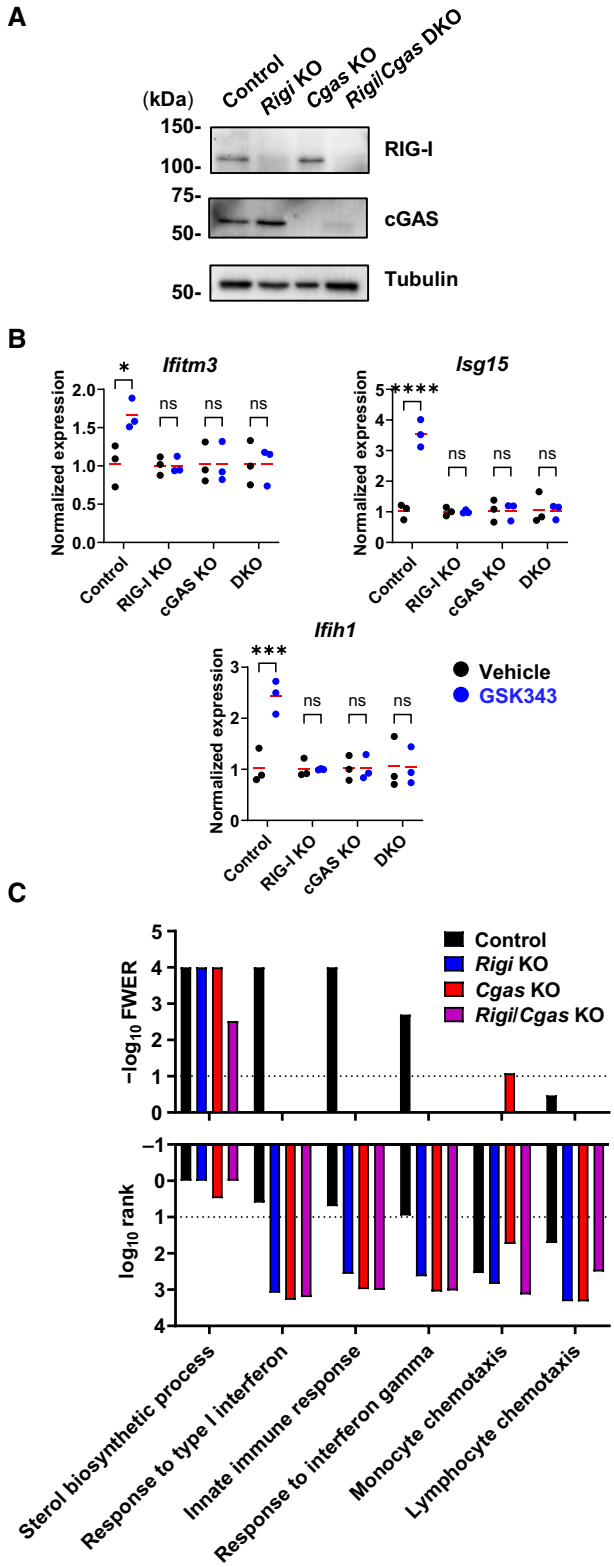

Figure 7. RIG-I and cGAS deletion blocks B16-F10 cells from upregulating IFN and innate immune genes and pathways upon GSK343 treatment.

A Western blots of control or KO cell pools.

B qRT–PCR quantification of three indicated ISGs upon GSK343 treatment compared to vehicle. B16-F10 cells were treated with DMSO or 2 μM GSK343 for 4 days (n = 3 biological replicates). Expression was normalized to the average of DMSO treatment within each genotype. *P < 0.05, ***P < 0.0005, ****P < 0.0001 by two-way ANOVA with Sidak's multiple test correction.

C Adjusted P values of indicated GO biological process gene sets for each cell line based on a weighted Kolmogorov–Smirnov statistic. Horizontal dotted line indicates cut-off at 0.1 (top). Position in ordered rank list of indicated GO biological processes gene sets for each cell line. Horizontal dotted line indicates the 10th rank (bottom).

Source data are available online for this figure.

We sought to understand the mechanism downstream of PRRs that upregulates chemotaxis-related genes. We observed that the NFκB family protein, p65, increased its chromatin binding upon GSK343 treatment in WT, but not RIC mutant B cells (Fig 6E). Therefore, we hypothesized that p65 was the mechanistic link between PRRs and gene expression as described above. To test this, we abrogated p65 activation by genetically deleting its upstream activator, IKKβ (Fig 6F). We confirmed successful deletion by western blotting (Fig 6G). As previously, we treated splenic B cells from these mice with GSK343 in culture, and quantified chemokine expression by qRT–PCR. In IKKβ KO B cells, *Ccl5*, *Ccl22* and *Cx3cl1*, were not significantly upregulated compared to controls (Fig 6H). *Ccl3*, however, was still upregulated despite inactivation of p65 signaling, indicating that IKKβ independent pathways also contribute.

Generation of IKKβ deficient B cells in this model required an interferon dependent *Mx-cre* inflammatory signaling mechanism induced by dsRNA polyIC administration. Since this chemical stimulant induces interferon, and B cells do not die, we also investigated gene expression in WT splenic B cells following polyIC treatment. This revealed clear activation of interferon stimulated genes *Isg15*, *Ifitm3*, and *Ifih1* (Fig EV4F), as well as chemokines identified above such as *Ccl3* and *Ccl5*. These observations further emphasize that GSK343 induced chemokine activation in B cells is distinct from interferon signaling.

EZH2 inhibition can induce multiple viral mimicry pathways

The lack of interferon and interferon stimulated gene (ISG) activation upon EZH2 inhibition and downstream PPR-dependent signaling contrasts with existing literature investigating its effects in cancer cells (Morel *et al*, 2021). Therefore, we sought to study the effect of EZH2 inhibition and the role of cytosolic PRRs in B16-F10 mouse melanoma cells, and to compare their gene expression changes to splenic B cells.

Using lentiviral transduction and CRISPR gene editing, we created cell populations that are either *Rigi*, *Cgas* or *Rigi/Cgas* double KO (Fig 7A). These cell lines were then treated with vehicle or 2 μM GSK343 for 4 days in culture. We extracted total RNA and performed qRT–PCR for three IFN-stimulated genes (ISGs). *Ifih1*, *Isg15*, and *Ifitm3* were significantly upregulated in control cells, but not in any of the three KO lines (Fig 7B). We performed RNA-seq and GSEA and compared with our B cell transcriptome data (Datasets EV3–EV6). In control cells, GSK343 treatment significantly upregulated pathways related to sterol metabolism and IFN

activation, but not chemokine or chemotaxis pathways (Fig 7C). In contrast, the sterol metabolic pathways were upregulated in all KO cells, but the IFN response pathways were not. We found that genes with a role in innate immune and IFN responses were among the most significantly upregulated genes in the control cells (Appendix Fig S2A), and these were essentially blocked in KO cells. Importantly, repetitive elements were comparably induced in all four cell lines by GSK343 treatment (Appendix Fig S2B). The contrast between gene expression changes upon the same EZH2 inhibition and PRR dependence in B16-F10 cells strongly suggests that the EBV infection-like viral mimicry response is unique to B cells.

Cytosolic PRRs mediate a cellular inflammatory response upon EZH2 inhibition

We next determined if PRRs control a cellular inflammatory response in the spleen in response to EZH2 inhibition. As before, we injected either vehicle or GSK343 daily for 2 days. We harvested the spleen and stained erythrocyte-lysed splenocytes with a multicolor antibody panel to identify key cell populations (Fig EV5A). $CD19^+$ staining of $CD45^+$ cells demonstrated that in WT spleens B cells were reduced nearly two-fold, but only modestly in the RIC mutants (Fig 8A). We also found that the proportion of $CD3^+$ T cells was increased upon GSK343 treatment in WT mice. However, this effect was also blunted in RIC mutants. Notably, the proportion of $CD8^+$ cytotoxic T cells among $CD3^+$ cells was increased in WT, but not significantly changed in RIC mutants upon EZH2 inhibition (Fig 8B). This suggests that in the absence of inflammatory cytokine signaling from RIC mutant B cells, they not only survive, but fail to recruit T effector cell populations.

We also quantified the proportion of myeloid cells in the spleen and found that $CD11b^+$ cells were significantly increased in WT spleens, but unchanged in RIC mutants (Fig 8C). More specifically, the increase in the proportion of $Ly6C^+$ $Ly6G^+$ neutrophils was significantly limited in the mutants (Fig 8C). We also measured absolute counts of each cell population per unit volume using counting beads. These data largely corroborate the proportions of cells described here (Fig EV5B). The significantly smaller proportions or absolute counts of $CD3^+CD8^+$ cytotoxic T cells, and $CD11b^+Ly6C^+Ly6G^+$ neutrophils in GSK343-treated RIC mutant spleens compared to WT implies that the inflammatory response in the mutants is greatly reduced.

Given EZH2's role in B lineage development we tested if GSK343 treatment in our 2-day experiments affected hematopoiesis. Staining and flow cytometry of bone marrow cells indicates that overall levels of CD19 and CD43 are unchanged in the course of experiments (Fig 8D). This suggests that GSK343 treatment does not alter progression of $CD43^+$ $CD19^-$ progenitors to $CD43^-$ $CD19^+$ immature B cell, nor does it increase $Ly6C^+$ $Ly6G^+$ neutrophils in the bone marrow (Fig 8D). This further suggests that the decrease in B cells or increase in neutrophils in the spleen upon GSK343 treatment is not due to similar changes in their production in the bone marrow during hematopoiesis. Overall, this flow cytometric analysis of splenic cells supports the conclusion that cytosolic PRRs mediate an inflammatory response upon EZH2 inhibition that attracts T cells and neutrophils, ultimately leading to B cell death.

Discussion

Our work demonstrates a central role for PRRs in responding to EZH2 inhibition in mammals. We revealed that EZH2 inhibition uniquely activates repetitive element expression in B cells. Repeat misexpression is detected in WT and RIC mutant B cells treated with EZH2 inhibitors, indicating that the functional loss of the PRRs does not compromise the initial, on-target effects of EZH2 inhibition. In contrast, loss of PRR function in RIC mutant B cells failed to activate expression of pro-inflammatory chemokines and inflammation and cell death were blocked. Based on these findings, we propose a signaling model in which EZH2 chemical inhibition induces a viral mimicry response leading to PRR and NFκB activation, chemokine expression, and B cell death through immune effector cells (Fig 9A and B). It is distinct from EZH2 inhibition in cancer cells that induces repeats and activates interferon signaling using the same PRRs (Fig 9C). This has important implications for EZH2 inhibitor use and it suggests new applications for this class of therapeutic.

Our H3K27me3 ChIP-seq data from B cells reveal a striking preference for EZH2 inhibition causing decreased H3K27me3 in intronic and intergenic regions in comparison with proximal promoters. Furthermore, our work reveals that there is extensive overlap of H3K27me3 intersecting with repetitive elements and EZH2 inhibitors induces their expression. In addition, we demonstrate that B cell repeat sequences lack CpG methylation. This unique combination of heterochromatin characteristics largely explains why B cells are susceptible to viral mimicry in response to EZH2 inhibitors. We are unaware of other cell types that possess this combination of chromatin characteristics as we did not detect this striking cell death and inflammation phenotype in other major organs or tissues.

Our data highlight the similarity between Epstein–Barr Virus infection and the response to EZH2 inhibitors that is best appreciated by the similarity of chemokines whose expression they both activate. Expression of *Csf1*, *Ccl22* (MDC), *Ccl1*, *Ccl3*, and *Ccl5* are all induced upon infection of B cells (Nakayama *et al*, 2004; Ehlin-Henriksson *et al*, 2009), and these chemokines are all activated in a

Figure 8. Cytosolic PRRs mediate GSK343-induced inflammation.

A–C WT and RIC mutant mice were I.P. injected with either vehicle or 100 mg/kg/day GSK343 for 2 days. Spleens were harvested and erythrocyte-lysed splenic lymphocytes were subjected to flow cytometry to quantify different immune cell populations. In each panel, a representative dot plot is shown for indicated cell populations under each treatment for WT and RIC mutant mice. Graphs below or adjacent summarize the proportions of each immune cell type as indicated (n = 7–10 biological replicates). Horizontal red bars represent the mean.

D WT mice were I.P. injected with either vehicle or 100 mg/kg/day GSK343 for 2 days. Erythrocyte-lysed bone marrow cells were subjected to flow cytometry to quantify different immune cell populations and analyzed as above (n = 5 biological replicates). Horizontal red bars represent the mean. *P < 0.05, **P < 0.01, ***P < 0.001, ****P < 0.0001 by two-way ANOVA with Tukey's multiple test correction.

Source data are available online for this figure.

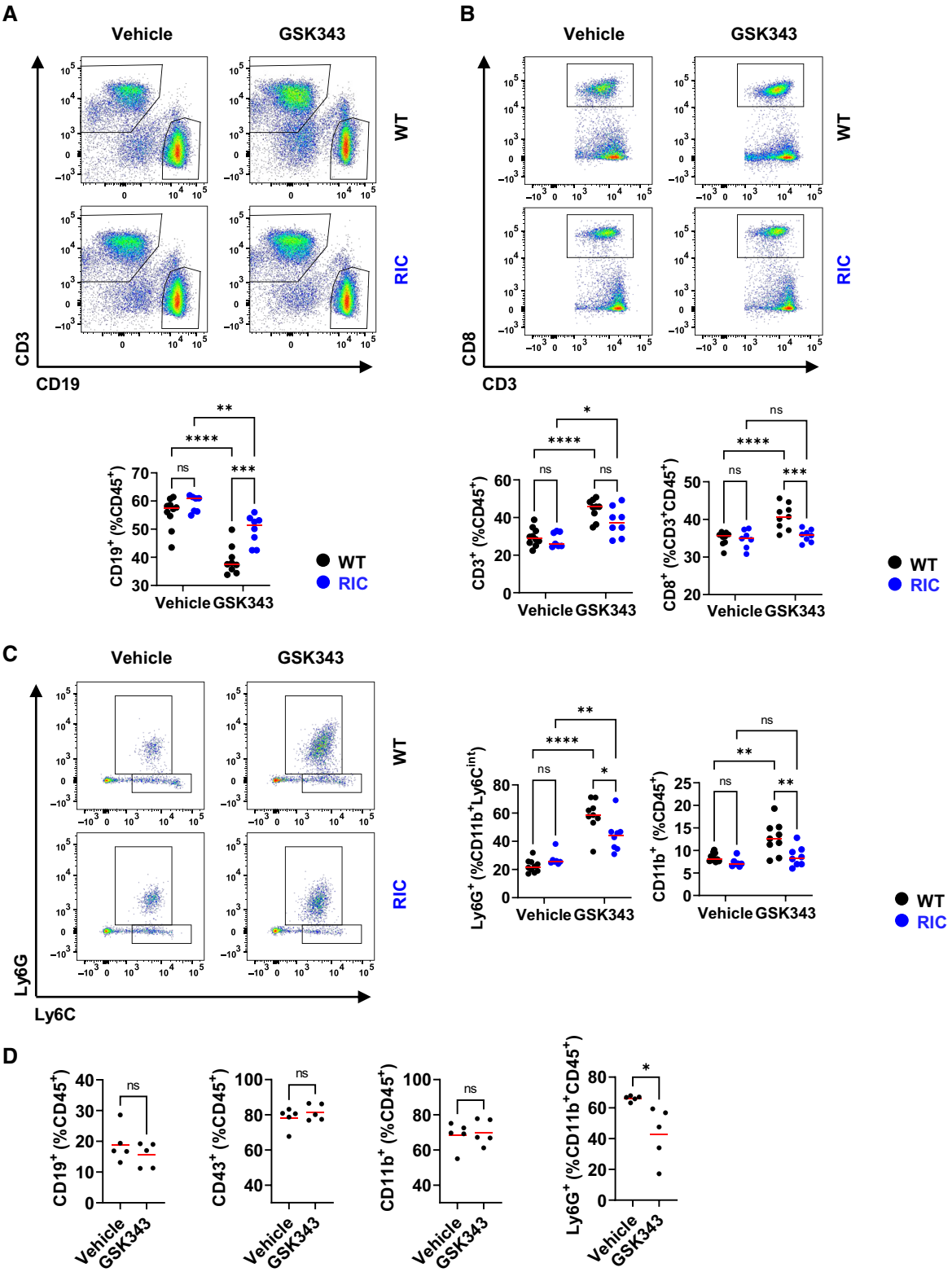

Figure 8.

PRR dependent manner by EZH2 inhibitors in our experiments. The mechanism by which B cell death is induced by EZH2 inhibitors likely depends on these chemokines and T cell recruitment. We expect this is distinct from the mechanism by which EBV encoded LMP1 activates a similar gene expression program during infection. Intriguingly, viral infection can activate repeat expression and NFκB

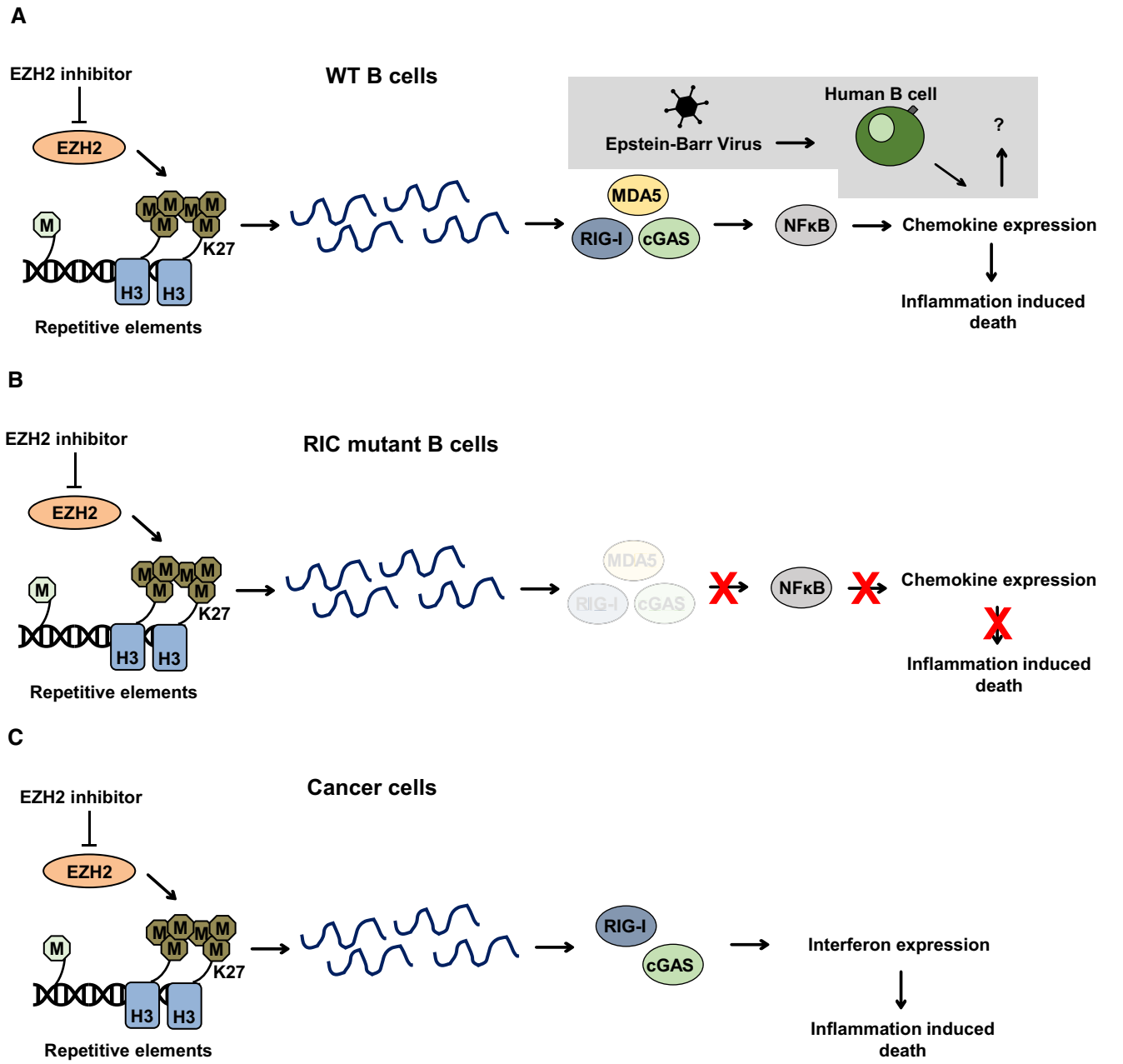

Figure 9. Models of viral mimicry in B cell and cancer cell contexts.

A, B Pathways of EZH2 inhibitors from their target to downstream components that contribute to inflammatory signaling. Intersection of EBV infection with chemokine expression program is shaded gray.

C Pathways of EZH2 inhibitor effects in cancer cells that induce interferon based inflammatory signaling.

suggesting viral infection may engage this pathway in unexpected ways (Jang & Latchman, 1989; Panning & Smiley, 1989, 1993; Williams *et al*, 2004; Karijolich *et al*, 2015). We compare gene expression programs with cell culture EBV-infected B cells, but note that some studies indicate that EBV-infected cells are targeted by T and NK cells following infection endogenously (Rickinson & Moss, 1997; Smith *et al*, 2009), suggesting there may be more similarities between EZH2 inhibition and EBV infection *in vivo*. Regardless of the precise explanation for B cell death, this viral mimicry that resembles EBV infection, reveals a distinct pathway activated by EZH2 not observed in prior studies of interferon activating paradigms described in cancer cells.

The rationale for generating EZH2 inhibitors is to counteract overactive H3K27me3 deposition that arises from overexpressed or mutationally activated EZH2. Our study reveals the consequence of inhibition of endogenous, wild type EZH2. We suggest important considerations and potential applications for EZH2 inhibitors in the future. First, short-term treatment with these inhibitors is capable of

inducing inflammation and depleting B cells. Recent studies using other EZH2 inhibitors, DZNep or GSK126, to treat mouse models of systemic lupus erythematosus demonstrated phenotypic improvement in a number of measures of disease pathology (Rohraff *et al*, 2019; Wu *et al*, 2021). These studies rationalized use of EZH2 inhibitors based on high level EZH2 expression even though this is not observed in all patients or relevant immune cell types. Our work demonstrates activation of viral mimicry in B cells after only brief treatment and suggests an alternate explanation to reduced B cells in these models. Secondly, the specificity of viral mimicry related immune stimulation in cancer treatment is based on the concept that cancer cells have precarious silencing of repeats. Epigenetic alterations inherent to cell transformation alter heterochromatin such that inhibitors of DNA methyltransferases selectively cause repeat expression in cancer cells but not normal somatic cells. Our work suggests that EZH2 inhibitors may be deployed based on a similar logic whereby low levels of DNA methylation are acquired through transformation and cells are susceptible to EZH2 inhibition even without overexpression of EZH2 (Morel *et al*, 2021). Our findings also raise the question of whether the activation of inflammatory signaling upon EZH2 inhibition in B cells from prolonged treatment with this class of inhibitor can lead to chronic inflammation. Overall, our work reveals a new effect of EZH2 inhibitors in immune function that is likely to have a significant impact on the use of these agents in clinical applications.

Materials and Methods

Mice

C57BL/6NCrl (Charles River, #027), B6.SJL-*Ptprc*^{a} *Pepc*^{b}/BoyJ (The Jackson Laboratory, #002014), B6.Cg-Tg(Mx1-cre)1Cgn/J; *Ikbkb*^{tm2Mka} (The Jackson Laboratory, #003556, Asfaha lab) and RIC triple mutant mice (described below) were housed and monitored according to institutional animal use guidelines (Western University, Animal Use Committee, protocol numbers 2020-039 and 2019-021). Mice were given access to standard chow and water *ad libitum* and exposed to 12 h light/dark cycles in a pathogen-free exclusion facility. For I.P. injections and splenic B cell isolation, littermates 6–8 week old mice of both sexes were randomly assigned to experimental groups within each genotype.

Intraperitoneal injections

For EZH2 inhibition *in vivo*, 6–8 week old mice were I.P injected daily with 100 mg/kg GSK343 (Tocris, #6128) for 2 or 5 days, UNC1999 (Cayman Chemical, #14621) for 2 days, or EPZ6438 (SelleckChem, #S7128) for 1 day in 20% (w/v) Captisol (Captisol, San Diego), pH 4.5 (with 1 N acetic acid). Control mice were I.P injected daily with 20% (w/v) Captisol (Captisol, San Diego), pH 4.5 (with 1 N acetic acid) for 2 or 5 days. Mice were sacrificed, and the spleen and bone marrow were harvested for analysis. For poly(I:C) (Millipore-Sigma, #P1530) treatment, 6–8 week old male or female WT and RIC mutant mice were I.P injected with either 100 μg poly (I:C) or PBS. To induce MDA5 expression as shown in Fig 3C, mice were injected once 24 h before harvesting the spleens. To quantify expression of ISGs and chemokines in splenic B cells as shown in Fig EV4E, mice were injected twice 48 h apart. To delete IKKβ as shown in Fig 6F, mice were injected three times every 48 h, then their spleens were harvested 1 week after the last injection. For adoptive transfer experiments, MACS-purified splenic B cells (2×10^7) from B6.SJL-*Ptprc*^{a} *Pepc*^{b}/BoyJ mice were I.P. injected into recipient C57BL/6NCrl mice 24 h before vehicle or GSK343 treatment.

Immunohistochemistry

Spleens were fixed in 10% neutral buffered formalin for 48 h prior to paraffin embedding. Routine H&E staining was performed. For immunohistochemistry, tissue sections were incubated in the following solutions for 3 min each: 100% xylene, 100% xylene, 100% ethanol, 100% ethanol, 95% ethanol, 70% ethanol. Antigen retrieval was performed in citrate (10 mM sodium citrate, pH 6.0) buffer for CD68 (Abcam, #125212, 1:100), and cleaved caspase 3 (CST, #9661, 1:400) staining. Slides were incubated with the primary antibodies in a humidified chamber overnight at 4°C. Goat anti-rabbit biotinylated IgG (VectorLabs, #BA-1000-1.5), peroxidase-streptavidin (VectorLabs, #SA-5704-100) and DAB substrate kit (VectorLabs, #SK-4100) were used the next day at RT to develop the staining. Mayer's hematoxylin was used to counterstain, then washed with tap water to destain. Slides were dehydrated and mounted with a coverslip and mounting medium (VectorLabs, #H-5000). DAB positive cell detection based on a maximum threshold in QuPath/0.3.2 was used to identify the percentage of cleaved caspase 3 positive cells. Object classifier was used to identify tingible body macrophages.

Cell culture

B16-F10 melanoma cells (ATCC, CRL-6475) were a gift from Dr. Charles Ishak. The cells were grown in DMEM (Wisent) supplemented with 10% (v/v) FBS, 2 mM L-glutamine, penicillin, and streptomycin at 37°C in 5% CO_2. For lentiviral transduction, HEK293T cells at 70% confluency on 6-well plates were transfected with 12 μg pLentiCRISPRv2 (Addgene, #52961, targeting cGAS, RIG-I or β-gal/luciferase), 9 μg pMD2.G (#12259) and 3 μg psPAX2 (#12260) using Lipofectamine 3000 (Life Technologies, #L3000001) following manufacturer's recommendations. After 48 h, the culture media were harvested and passed through a 0.45 μm filter. B16-F10 cells were transduced with the appropriate filtrate containing 8 μg/ml polybrene. To select for transduced cells, B16-F10 cells were maintained in media containing 1 μg/ml puromycin. To isolate cGAS/RIG-I single, or double KO cells, puromycin-selected cells were seeded on 96-well plates at low density, and subpopulations were tested for protein expression by Western blotting. Those with confirmed loss of cGAS/RIG-I expression were pooled together for subsequent experiments. Identities of B16-F10 cells and engineered variants were confirmed by western blotting and cells were tested for mycoplasma contamination.

For GSK343 treatment, B16-F10 cells (3×10^5) were seeded on 6-well plates. Next day, DMSO or 2 μM GSK343 were added, and the cells were treated for 4 days. Culture media were replaced daily.

For splenocyte culture, spleens were harvested from untreated WT and RIC mutant mice, gently homogenized with a syringe plunger and passed through a 40 μm mesh filter (Fisher Scientific,

#08-771-1). Filtered cells were centrifuged at 300 *g* for 10 min at 4°C. The cell pellet was resuspended in ACK lysis buffer (150 mM NH_4Cl, 10 mM $KHCO_3$, 0.1 mM EDTA, pH 7.2) for 4 min at RT to lyse erythrocytes. Remaining splenic lymphocytes were washed twice with FACS buffer (5% BSA, 2 mM EDTA in PBS) and incubated in RPMI-1640 (Wisent) supplemented with 10% (v/v) FBS, 55 μM 2-ME, 2 mM L-glutamine, penicillin and streptomycin at 37°C in 5% CO_2.

To isolate splenic B cells and $CD43^+$ cells, washed splenic lymphocytes (5×10^7) were resuspended in 450 μl FACS buffer and stained with 50 μl CD43 microbeads (Miltenyi Biotec, #130-049-801) at 4°C for 30 min. Cells were washed once, resuspended in 500 μl FACS buffer and passed through an LD column in a VarioMACS separator (Miltenyi Biotec, #130-042-901, #130-090-282) as per manufacturer's recommendations. CD43 microbead-labeled $CD43^+$ cells were eluted from the column by applying the plunger. Purified B cells or $CD43^+$ cells were incubated in RPMI-1640 supplemented as above plus 2 ng/ml IL-4 and 2 ng/ml BAFF (BioLegend, #574302, #591202) at 37°C in 5% CO_2 for all *ex vivo* experiments. These cells were treated with DMSO, GSK343 (Tocris, #6128), UNC1999 (Cayman Chemical, #14621) or EPZ6438 (SelleckChem, #S7128) for 48 h in culture. Cell viability was measured by trypan blue exclusion assay and quantified by Countess II (ThermoFisher).

Infinium mouse methylation array

Genomic DNA was purified from B or $CD43^+$ cells using Monarch genomic DNA purification kit (NEB, #T3010). Further sample processing and mouse methylation array (Illumina) were performed by The Centre for Applied Genomics, The Hospital for Sick Children, Toronto, Canada. "Combined rank" metric in RnBeads/3.17 was used to generate an ordered list of differentially methylated probes between DMSO-treated B and $CD43^+$ cells (Müller *et al*, 2019). In addition to default probe annotations (cpgislands, genes, and promoters), a custom repClass annotation was generated from RepeatMasker (downloaded from UCSC table browser) and applied to the probes. Beta values of such annotated, differentially methylated probes were represented as heatmaps (gplots /3.1.3).

RNA extraction, qRT–PCR and sequencing

Splenocytes or splenic B cells (5×10^6 cells/ml) were treated with either DMSO or 1 μM GSK343 for 48 h. RNA was harvested using Monarch Total RNA miniprep kit (NEB, #T2010) and residual genomic DNA was digested by treating 1 μg total RNA with 1 U DNaseI (ThermoFisher, #18068015) for 15 min at RT. DNaseI was then inactivated by adding EDTA and incubating at 65°C for 10 min. For qRT–PCR, RNA was then reverse-transcribed into cDNA with iScript Supermix (Biorad, #1708840) and diluted five-fold with H_2O. PCR was performed with iQ SYBR Green Supermix (Biorad, #1708882) on CFX96 (Biorad). All primer sequences are described in Table EV5 (Stetson & Medzhitov, 2006). For sequencing, DNaseI-treated RNA was purified with Monarch RNA cleanup kit (NEB, #T2040). rRNA depletion and library preparation were performed with VAHTS total RNA-seq library prep kit (GeneBio, #NR603-01). Libraries were pooled and sequenced on NextSeq 500 at the London Regional Genomics Center with a high output 75 cycle kit to yield single-end 75-bp reads.

RNA sequencing analysis

Demultiplexed FASTQ files were downloaded from BaseSpace. RepEnrich2 and featureCounts were used to quantify repetitive element expression (Criscione *et al*, 2014; Liao *et al*, 2014; Teissandier *et al*, 2019). Briefly, bowtie2/2.4.2 (Langmead & Salzberg, 2012) was used to map reads to mm10 with default settings. Resulting sam files were converted to bam files with samtools/1.12 (Li *et al*, 2009). RepeatMasker track for mm10 was filtered to remove simple repeats, then used to build a pseudogenome with RepEnrich2 subcommands. Fractional count tables were imported to Rstudio running r/3.6.3. Alternatively, STAR/2.5.2b (Dobin *et al*, 2013) and featureCounts were used with recommended settings (Teissandier *et al*, 2019) with the filtered RepeatMasker track to generate count tables. For gene expression quantification, reads were mapped to mm10 genome with STAR/2.7.8a and resulting sam files were converted to sorted, indexed bam files with samtools/1.12. HTSeq/0.11.0 (Anders *et al*, 2015) was used to assign mapped reads to GENCODE mouse M22 comprehensive gene annotation (Frankish *et al*, 2019).

To identify differentially expressed repetitive elements or genes, edgeR/3.28.1 (Robinson *et al*, 2010) was used with default Benjamini-Hochberg *P*-value adjustment. Volcano plots, heatmaps, and Venn diagrams were generated with EnhancedVolcano, heatmap.2 and VennDiagram, respectively (Chen & Boutros, 2011). GSEA was performed as recommended using a weighted Kolmogorov–Smirnov statistic (Mootha *et al*, 2003; Subramanian *et al*, 2005). Upset plot was generated using UpSetR/1.4.0.

ChIP sequencing

WT and RIC mutant splenic B cells (5×10^6 cells/ml, 7.5×10^6 cells total) were treated with either DMSO or 1 μM GSK343 for 48 h. Cells were washed with PBS and resuspended in 1 ml 1% (v/v) formaldehyde in PBS to fix chromatin-protein complexes. After 5 min, the reaction was quenched by adding glycine to a final concentration of 0.125 M. Fixed cells were washed twice with PBS and incubated on ice for 10 min in lysis buffer 1 (10 mM HEPES pH 6.5, 10 mM EDTA, 0.5 mM EGTA, 0.25% Triton X-100). The suspension was centrifuged at 600 *g* for 5 min at 4°C to isolate the nuclei. They were washed twice in wash buffer (10 mM HEPES pH 6.5, 1 mM EDTA, 0.5 mM EGTA, 200 mM NaCl) and resuspended in lysis buffer 2 (50 mM Tris pH 8.0, 1 mM EDTA, 0.5% Triton X-100, 1% SDS) to 7.5×10^6 cell/200 μl in sonication tubes. The following protease inhibitors were added immediately before use to all of the above buffers: 250 μM Na_3VO_4, 1 mM NaF, 0.1 mM PMSF, 5 μg/ml aprotinin and leupeptin. DNA yield was quantified with Qubit fluorometer (ThermoFisher). Chromatin was sonicated to 100–600 bp fragments by four cycles of 30 s ON and OFF in Bioruptor Pico (Diagenode, #B01060010). Debris was cleared by centrifugation at 16,000 *g* for 30 min at 4°C. Then, chromatin was pre-cleared with 30 μl Dynabeads Protein G (ThermoFisher, #10004D) by gentle end-to-end mixing at 4°C for 2 h. Pre-cleared chromatin was diluted 10-fold in dilution buffer (50 mM Tris pH 8.0, 1 mM EDTA, 150 mM NaCl, 0.1% Triton X-100) and 5% (by volume) was saved as input until later. H3K27me3 antibody (4 μg, Millipore-Sigma, #07-449) was added to pre-cleared chromatin (30 μg) and mixed end-to-end at 4°C overnight. The next day, antibody-chromatin complexes were

captured by adding 50 µl Dynabeads Protein G and gentle end-to-end mixing at 4°C for 2 h. They were washed once with low salt buffer (20 mM Tris pH 8.0, 2 mM EDTA, 150 mM NaCl, 1% Triton X-100, 0.1% SDS), once with high salt buffer (20 mM Tris pH 8.0, 2 mM EDTA, 500 mM NaCl, 1% Triton X-100, 0.1% SDS), once with LiCl wash buffer (10 mM Tris pH 8.0, 1 mM EDTA, 0.25 M LiCl, 1% NP-40, 1% sodium deoxycholate) and twice with TE buffer (10 mM Tris pH 8.0, 1 mM EDTA). For each wash, the immunoprecipitated complexes were mixed end-to-end at 4°C for 5 min. Antibody-chromatin complexes were eluted from Dynabeads by incubating in elution buffer (0.1 M $NaHCO_3$, 1% SDS) at 65°C and vortexing. To the elution (ChIP) and input (saved earlier), NaCl was added to a final concentration of 200 mM to reverse crosslinked protein-DNA complexes and incubated overnight at 65°C. The next day, the suspension was mixed with RNaseA and proteinase K to digest RNA and proteins, respectively, and incubated at 45°C. Finally, ChIP and input chromatin were purified with Monarch PCR/DNA cleanup kit (NEB, #T1030) and eluted with H_2O. Following the manufacturer's recommendation, input (25 ng) or ChIP (0.5 ng) DNA were used to perform end repair, adaptor ligation, and PCR amplification with NEBNext Ultra II DNA library prep kit and Multiplex Oligos (NEB, #E7645, #E7600). AmpureXP beads (Beckman Coulter, #A63880) were used at 0.9–1.0× reaction volumes for size selection. Input or ChIP samples were amplified by 10 or 15 PCR cycles, respectively, which yielded ~ 600 ng DNA. Libraries were pooled and sequenced on NextSeq 500 at the London Regional Genomics Center with a high output 75 cycle kit to yield paired-end 38-bp read pairs.

ChIP sequencing analysis

Demultiplexed FASTQ files were downloaded from BaseSpace. First, ENCODE blacklist regions (Amemiya *et al*, 2019) were filtered out from subsequent analysis. Reads were mapped to mm10 genome with bowtie2/2.4.2 with sensitive-local setting. Samtools/1.12 was used with -f 0x2 option to keep concordantly mapped read pairs. Those read pairs were converted to sorted, indexed bam files. Biological duplicates were pooled together and MACS2/2.2.7.1 (Zhang *et al*, 2008) was used to call broad peaks, outputting broadPeak files. A subcommand of deepTools/3.5.1 (Ramírez *et al*, 2016), bamCoverage, was used to generate reads-per-genomic-content (RPGC) normalized signal track (bw files) for all sequenced libraries. To account for composition biases in ChIP libraries, the trimmed mean of M-values method available in csaw/1.32.0 was used to generate scaling factors, which were passed into bamCoverage subcommand with scaleFactor (Lun & Smyth, 2016a, 2016b). csaw was also used to quantify the loss of H3K27me3 at regions near genes and promoters upon GSK343 treatment compared to vehicle. plotEnrichment, computeMatrix, plotHeatmap, and plotProfile commands (deepTools/3.5.1) were used to make barplots, heatmaps, and profiles. Bedtools/2.30.0 (Quinlan & Hall, 2010) was used to find peaks or number of peaks that intersected with RepeatMasker features, or were unique or common between treatment conditions or genotypes. ChIPseeker (Yu *et al*, 2015) was used to annotate peaks based on known genomic features. To show read mapping (color-coded by strand) in Fig EV3B, samtools/1.12 was used with -f 0x40 option to split read pairs into two bam files. A bam file of one of the read mates (a ChIP sample of DMSO-treated WT B cells) was imported to IGV/2.11.1 (Robinson *et al*, 2011) to show mapped reads at two loci. To show H3K27me3 signal enrichment at indicated loci (RPGC), bw files of biological replicates were merged together with bigWigMerge and bedGraphToBigWig (Kent *et al*, 2010). Merged signal track and broadPeak files were visualized on IGV/2.11.1. Peaks with a score < 20 were filtered out.

Flow cytometry

Total splenocytes or bone marrow cells were isolated as described above. 2×10^6 cells were resuspended in PBS with ZombieNIR (1:500, BioLegend, #423105) and incubated on ice for 30 min to stain dead cells. Then, they were washed with FACS buffer and resuspended in pre-staining mix containing 50 µl Brilliant Stain Buffer (BD Biosciences, #563794), 5 µl TruStain monocyte blocker (BioLegend, #426102), 1 µl TruStain FcX plus (BioLegend, #156603) and 27.4 µl FACS buffer. Splenocytes were stained with the following antibody cocktail: anti-CD45.2 BV421 (BioLegend, #109831), anti-CD19 BV510 (BioLegend, #115545), anti-Ly6C BV605 (BioLegend, #128035), anti-CD11b FITC (BioLegend, #101206), anti-CD3ε PerCP/Cy5.5 (BioLegend, #100327), anti-CD8α PE (BioLegend, #100707), anti-CD45.1 PE/Dazzle 594 (BioLegend, #110747) and anti-Ly6G APC (BioLegend, #127613). Bone marrow cells were stained with a similar panel but with the following substitution: anti-CD43 PerCP/Cy5.5 (BioLegend, #143219) and anti-CD45R PE (BioLegend, #103207). Stained cells were kept on ice for 30 min, then washed with FACS buffer. Cells were fixed in 100 µl fixation buffer (BD Biosciences, #554655) on ice for 20 min. They were washed and resuspended in 500 µl FACS buffer and 100 µl Precision counting beads (BioLegend, #424902). Flow cytometry was performed on LSR II (BD Biosciences) at the London Regional Flow Cytometry Facility and analyzed with FlowJo/10.8.1. AbC total antibody compensation beads and ArC amine reactive compensation beads (ThermoFisher, #A10497, #A10628) were used to generate compensation matrices in FACSDiva (BD Biosciences).

Protein extraction and pulldown assay

Erythrocyte-lysed splenocytes were lysed in RIPA buffer (50 mM Tris pH 7.4, 150 mM NaCl, 1% NP-40, 0.5% sodium deoxycholate, 0.1% SDS, supplemented with protease inhibitors as above) on ice for 10 min. Chromatin fractions were prepared by lysing cells sequentially in buffer A (10 mM Tris pH 8.0, 10 mM KCl, 1.5 mM $MgCl_2$, 0.34 M sucrose, 10% (v/v) glycerol, 0.1% Triton-X, supplemented with protease inhibitors as above), then in buffer B (3 mM EDTA, 0.2 mM EGTA, supplemented with protease inhibitors as above) with occasional mixing. Cytoplasmic and nucleoplasmic fractions were discarded by centrifugation, and resulting chromatin was digested with DNaseI in digestion buffer (20 mM Tris pH 7.5, 10 mM $MgCl_2$).

For cGAS pulldown assay, erythrocyte-lysed splenocytes were lysed in non-ionic buffer (25 mM HEPES, 100 mM NaCl, 1 mM EDTA, 10% (v/v) glycerol, 1% Triton X-100, supplemented with protease inhibitors as above) on ice for 10 min. Debris was cleared by centrifugation at 16,000 *g* for 30 min at 4°C. Bradford assays were used to quantify protein concentration. For the pulldown assay, 500 µg of extract was mixed with 400 pmol of 5′

biotinylated ISD45 dsDNA and gently mixed end-to-end overnight at 4°C. The next day, 20 µl streptavidin Dynabeads (ThermoFisher, #11205D) were added and gently mixed for 2 h at 4°C. Pulldown complexes were washed once with non-ionic lysis buffer and once with non-ionic lysis buffer supplemented with 300 mM NaCl.

For histone acid extraction, purified, cultured splenic B cells were lysed in buffer (PBS, 0.5% Triton X-100, supplemented with protease inhibitors as above) on ice with gentle mixing for 10 min. Nuclei were isolated by centrifugation at 2,000 rpm for 10 min at 4°C. The pellet was resuspended in 0.4 N HCl overnight at 4°C. Next day, cell debris was cleared by centrifugation, and trichloroacetic acid (1/3 volume) was added to the supernatant, and kept on ice for 2 h. Precipitated histones were washed twice with 0.1% HCl (v/v) in cold acetone, then cold acetone. Residual acetone was removed by incubation at 55°C. Histone pellet was resuspended in water before quantification with Bradford assays.

SDS–PAGE and Western blot

RIPA extracts, histone extracts or pulldown samples were denatured by adding Laemmli buffer to 1× and boiling at 95°C for 5 min. SDS–PAGE was performed following standard procedures. Samples were transferred to PVDF membrane using TransBlot Turbo (Biorad) and blocked in 5% skim milk in TBST for 1 h at RT. Membranes were incubated overnight at 4°C with gentle shaking with the following primary antibodies: α- tubulin (CST, #2125, 1:5,000), cGAS (CST, #31659, 1:1,000), MDA5 (CST, #5321, 1:1,000), RIG-I (Santa Cruz, #376845, 1:1,000), H3K27me3 (CST, #9733, 1:3,000), total H3 (Abcam, #ab1791, 1:5,000), p65 (CST, #8242, 1:2,000), IKKβ (CST, ##8,943, 1:2,000), GAPDH (CST, #2188, 1:4,000). The next day, membranes were washed five times with TBST and incubated with the following secondary antibodies for 1 h at RT with gentle shaking: m-IgG Fc BP-HRP (Santa Cruz, #525409, 1:500) or AffiniPure goat anti-rabbit IgG-HRP (JIR, #111-035-144, 1:5,000–10,000). After five washes with TBST, membranes were incubated in SuperSignal WestDura (ThermoFisher, #34075) and visualized on a ChemiDoc (Biorad). Coomassie staining was performed with GelCode Blue (ThermoFisher, #24590). Image Lab/6.1.0 was used to capture images, detect lanes, and quantify H327me3 or H3 bands for densitometry analysis.

CRISPR-Cas9 generation of RIC mutant mice

In vitro production of gRNAs and one-cell embryo injection were all performed as previously described (Wang *et al*, 2013), by the London Regional Transgenic and Gene Targeting Facility. C57BL/6Crl mice were used as embryo donors, surrogate females and stud males. For restriction fragment length polymorphism assays, each of the three target loci was PCR amplified from tail DNA with Phire Animal Tissue Direct PCR kit (ThermoFisher, #F140WH). These products were either left undigested or restriction digested with the indicated enzymes and resolved on an agarose gel and EtBr stained. PCR reactions were also cloned into a plasmid and Sanger sequencing was performed to find the exact deletions in all mutant alleles present in the colony (Appendix Table S1). In addition, potential off-target sites were predicted *in silico* (Cradick *et al*, 2014) and the two highest ranked intergenic and intragenic loci were genotyped through PCR amplification and sequencing (Appendix Table S2).

Quantification and statistical analysis

All statistical analyses were performed with Prism 9. All relevant details are described in the figure legends.

Data availability

The datasets produced in this study are available in the SuperSeries (GSE198232, https://www.ncbi.nlm.nih.gov/geo/query/acc.cgi?acc=GSE198232) which contains the following SubSeries:

- RNA-seq data: Gene Expression Omnibus GSE198159 (https://www.ncbi.nlm.nih.gov/geo/query/acc.cgi?acc=GSE198159), Gene Expression Omnibus GSE239879 (https://www.ncbi.nlm.nih.gov/geo/query/acc.cgi?acc=GSE239879).
- ChIP-seq data: Gene Expression Omnibus GSE198158 (https://www.ncbi.nlm.nih.gov/geo/query/acc.cgi?acc=GSE198158).
- Infinium methylation data: Gene Expression Omnibus GSE229684 (https://www.ncbi.nlm.nih.gov/geo/query/acc.cgi?acc=GSE229684).

RNA-seq data of EBV-infected human B cells was obtained from GEO under GSE125974 (https://www.ncbi.nlm.nih.gov/geo/query/acc.cgi?acc=GSE125974) (Data ref: Wang *et al*, 2019b). Original Western blot images have been submitted to the journal as source files. This paper does not report original code. Any additional information required to reanalyze the data reported in this paper is available from the lead contact upon request. B16-F10 cell lines generated in this study are available from the lead contact upon request. RIC mice are available from The Jackson Laboratory as Stock No. 039010.

Expanded View for this article is available online.

Acknowledgements
The authors are grateful to Drs. Nathalie Berube and Lisa Cameron for advice in preparing this manuscript. SJK was funded by the Cancer Research and Technology Transfer training program and an Ontario Graduate Scholarship. This work was supported by a grant from the Canadian Institute of Health Research (PJT-156014) to FAD. The authors wish to thank numerous colleagues at the London Regional Cancer Program for suggestions and encouragement in the course of this work.

Author contributions
Frederick A Dick: Conceptualization; funding acquisition; methodology; writing – original draft; project administration; writing – review and editing. **Seung J Kim:** Conceptualization; data curation; formal analysis; investigation; visualization; methodology; writing – original draft; writing – review and editing. **Patti K Kiser:** Formal analysis; methodology; writing – original draft. **Rodney P DeKoter:** Conceptualization; resources; methodology. **Samuel Asfaha:** Resources; methodology.

Disclosure and competing interests statement
The authors declare that they have no conflict of interest.

References

Amemiya HM, Kundaje A, Boyle AP (2019) The ENCODE blacklist: identification of problematic regions of the genome. *Sci Rep* 9: 9354

Anders S, Pyl PT, Huber W (2015) HTSeq—a Python framework to work with high-throughput sequencing data. *Bioinformatics* 31: 166 – 169

Babaian A, Mager DL (2016) Endogenous retroviral promoter exaptation in human cancer. *Mob DNA* 7: 24

Béguelin W, Rivas MA, Calvo Fernández MT, Teater M, Purwada A, Redmond D, Shen H, Challman MF, Elemento O, Singh A *et al* (2017) EZH2 enables germinal centre formation through epigenetic silencing of CDKN1A and an Rb-E2F1 feedback loop. *Nat Commun* 8: 877

Béguelin W, Teater M, Meydan C, Hoehn KB, Phillip JM, Soshnev AA, Venturutti L, Rivas MA, Calvo-Fernández MT, Gutierrez J *et al* (2020) Mutant EZH2 induces a pre-malignant lymphoma niche by reprogramming the immune response. *Cancer Cell* 37: 655 – 673

Bulut-Karslioglu A, De La Rosa-Velázquez IA, Ramirez F, Barenboim M, Onishi-Seebacher M, Arand J, Galán C, Winter GE, Engist B, Gerle B *et al* (2014) Suv39h-dependent H3K9me3 marks intact retrotransposons and silences line elements in mouse embryonic stem cells. *Mol Cell* 55: 277 – 290

Cao R, Wang L, Wang H, Xia L, Erdjument-Bromage H, Tempst P, Jones RS, Zhang Y (2002) Role of histone H3 lysine 27 methylation in polycomb-group silencing. *Science* 298: 1039 – 1043

Chen H, Boutros PC (2011) VennDiagram: a package for the generation of highly-customizable Venn and Euler diagrams in R. *BMC Bioinformatics* 12: 35

Chen R, Ishak CA, De Carvalho DD (2021) Endogenous retroelements and the viral mimicry response in cancer therapy and cellular homeostasis. *Cancer Discov* 11: 2707 – 2725

Chiappinelli KB, Strissel PL, Desrichard A, Li H, Henke C, Akman B, Hein A, Rote NS, Cope LM, Snyder A *et al* (2015) Inhibiting DNA methylation causes an interferon response in cancer via dsRNA including endogenous retroviruses. *Cell* 162: 974 – 986

Collinson A, Collier AJ, Morgan NP, Sienerth AR, Chandra T, Andrews S, Rugg-Gunn PJ (2016) Deletion of the polycomb-group protein EZH2 leads to compromised self-renewal and differentiation defects in human embryonic stem cells. *Cell Rep* 17: 2700 – 2714

Cradick TJ, Qiu P, Lee CM, Fine EJ, Bao G (2014) COSMID: a web-based tool for identifying and validating CRISPR/Cas off-target sites. *Mol Ther Nucleic Acids* 3: e214

Criscione SW, Zhang Y, Thompson W, Sedivy JM, Neretti N (2014) Transcriptional landscape of repetitive elements in normal and cancer human cells. *BMC Genomics* 15: 583

Day DS, Luquette LJ, Park PJ, Kharchenko PV (2010) Estimating enrichment of repetitive elements from high-throughput sequence data. *Genome Biol* 11: R69

Dellino GI, Schwartz YB, Farkas G, McCabe D, Elgin SCR, Pirrotta V (2004) Polycomb silencing blocks transcription initiation. *Mol Cell* 13: 887 – 893

Desai N, Sajed D, Arora KS, Solovyov A, Rajurkar M, Bledsoe JR, Sil S, Amri R, Tai E, MacKenzie OC *et al* (2017) Diverse repetitive element RNA expression defines epigenetic and immunologic features of colon cancer. *JCI Insight* 2: e91078

Dobin A, Davis CA, Schlesinger F, Drenkow J, Zaleski C, Jha S, Batut P, Chaisson M, Gingeras TR (2013) STAR: ultrafast universal RNA-seq aligner. *Bioinformatics* 29: 15 – 21

Doucet-O'Hare TT, Rodić N, Sharma R, Darbari I, Abril G, Choi JA, Ahn JY, Cheng Y, Anders RA, Burns KH *et al* (2015) LINE-1 expression and retrotransposition in Barrett's esophagus and esophageal carcinoma. *Proc Natl Acad Sci USA* 112: E4894 – E4900

Ehlin-Henriksson B, Liang W, Cagigi A, Mowafi F, Klein G, Nilsson A (2009) Changes in chemokines and chemokine receptor expression on tonsillar B cells upon Epstein-Barr virus infection. *Immunology* 127: 549 – 557

Eskeland R, Leeb M, Grimes GR, Kress C, Boyle S, Sproul D, Gilbert N, Fan Y, Skoultchi AI, Wutz A *et al* (2010) Ring1B compacts chromatin structure and represses gene expression independent of histone ubiquitination. *Mol Cell* 38: 452 – 464

Ewing AD, Gacita A, Wood LD, Ma F, Xing D, Kim M-S, Manda SS, Abril G, Pereira G, Makohon-Moore A *et al* (2015) Widespread somatic L1 retrotransposition occurs early during gastrointestinal cancer evolution. *Genome Res* 25: 1536 – 1545

Francis NJ, Kingston RE, Woodcock CL (2004) Chromatin compaction by a polycomb group protein complex. *Science* 306: 1574 – 1577

Frankish A, Diekhans M, Ferreira A-M, Johnson R, Jungreis I, Loveland J, Mudge JM, Sisu C, Wright J, Armstrong J *et al* (2019) GENCODE reference annotation for the human and mouse genomes. *Nucleic Acids Res* 47: D766 – D773

Goubau D, Deddouche S, Reis e Sousa C (2013) Cytosolic sensing of viruses. *Immunity* 38: 855 – 869

Hansen K, Prabakaran T, Laustsen A, Jørgensen SE, Rahbæk SH, Jensen SB, Nielsen R, Leber JH, Decker T, Horan KA *et al* (2014) Listeria monocytogenes induces IFNβ expression through an IFI16-, cGAS- and STING-dependent pathway. *EMBO J* 33: 1654 – 1666

Howard G, Eiges R, Gaudet F, Jaenisch R, Eden A (2008) Activation and transposition of endogenous retroviral elements in hypomethylation induced tumors in mice. *Oncogene* 27: 404 – 408

Ishak CA, De Carvalho DD (2020) Reactivation of endogenous retroelements in cancer development and therapy. *Annu Rev Cancer Biol* 4: 159 – 176

Ishak CA, Marshall AE, Passos DT, White CR, Kim SJ, Cecchini MJ, Ferwati S, MacDonald WA, Howlett CJ, Welch ID *et al* (2016) An RB-EZH2 complex mediates silencing of repetitive DNA sequences. *Mol Cell* 64: 1074 – 1087

Jang KL, Latchman DS (1989) HSV infection induces increased transcription of Alu repeated sequences by RNA polymerase III. *FEBS Lett* 258: 255 – 258

Karijolich J, Abernathy E, Glaunsinger BA (2015) Infection-induced retrotransposon-derived noncoding RNAs enhance herpesviral gene expression via the NF-κB pathway. *PLoS Pathog* 11: e1005260

Karimi MM, Goyal P, Maksakova IA, Bilenky M, Leung D, Tang JX, Shinkai Y, Mager DL, Jones S, Hirst M *et al* (2011) DNA methylation and SETDB1/H3K9me3 regulate predominantly distinct sets of genes, retroelements, and chimeric transcripts in mESCs. *Cell Stem Cell* 8: 676 – 687

Karolchik D, Hinrichs AS, Furey TS, Roskin KM, Sugnet CW, Haussler D, Kent WJ (2004) The UCSC Table Browser data retrieval tool. *Nucleic Acids Res* 32: D493 – D496

Kent WJ, Zweig AS, Barber G, Hinrichs AS, Karolchik D (2010) BigWig and BigBed: enabling browsing of large distributed datasets. *Bioinformatics* 26: 2204 – 2207

Kleer CG, Cao Q, Varambally S, Shen R, Ota I, Tomlins SA, Ghosh D, Sewalt RGAB, Otte AP, Hayes DF *et al* (2003) EZH2 is a marker of aggressive breast cancer and promotes neoplastic transformation of breast epithelial cells. *Proc Natl Acad Sci USA* 100: 11606 – 11611

Kondo Y, Issa J-PJ (2003) Enrichment for histone H3 lysine 9 methylation at Alu repeats in human cells. *J Biol Chem* 278: 27658 – 27662

de Koning APJ, Gu W, Castoe TA, Batzer MA, Pollock DD (2011) Repetitive elements may comprise over two-thirds of the human genome. *PLoS Genet* 7: 1002384

Ku M, Koche RP, Rheinbay E, Mendenhall EM, Endoh M, Mikkelsen TS, Presser A, Nusbaum C, Xie X, Chi AS *et al* (2008) Genomewide analysis of PRC1

and PRC2 occupancy identifies two classes of bivalent domains. *PLoS Genet* 4: e1000242

Kuzmichev A, Nishioka K, Erdjument-Bromage H, Tempst P, Reinberg D (2002) Histone methyltransferase activity associated with a human multiprotein complex containing the enhancer of zeste protein. *Genes Dev* 16: 2893 – 2905

Lamprecht B, Walter K, Kreher S, Kumar R, Hummel M, Lenze D, Köchert K, Bouhlel MA, Richter J, Soler E *et al* (2010) Derepression of an endogenous long terminal repeat activates the CSF1R proto-oncogene in human lymphoma. *Nat Med* 16: 571 – 579

Langmead B, Salzberg SL (2012) Fast gapped-read alignment with Bowtie 2. *Nat Methods* 9: 357 – 359

Leeb M, Pasini D, Novatchkova M, Jaritz M, Helin K, Wutz A (2010) Polycomb complexes act redundantly to repress genomic repeats and genes. *Genes Dev* 24: 265 – 276

Levin HL, Moran JV (2011) Dynamic interactions between transposable elements and their hosts. *Nat Rev Genet* 12: 615 – 627

Li H, Handsaker B, Wysoker A, Fennell T, Ruan J, Homer N, Marth G, Abecasis G, Durbin R, 1000 Genome Project Data Processing Subgroup (2009) The Sequence Alignment/Map format and SAMtools. *Bioinformatics* 25: 2078 – 2079

Liao Y, Smyth GK, Shi W (2014) featureCounts: an efficient general purpose program for assigning sequence reads to genomic features. *Bioinformatics* 30: 923 – 930

Liu S, Brind'Amour J, Karimi MM, Shirane K, Bogutz A, Lefebvre L, Sasaki H, Shinkai Y, Lorincz MC (2014) Setdb1 is required for germline development and silencing of H3K9me3-marked endogenous retroviruses in primordial germ cells. *Genes Dev* 28: 2041 – 2055

Liu M, Thomas SL, DeWitt AK, Zhou W, Madaj ZB, Ohtani H, Baylin SB, Liang G, Jones PA (2018) Dual inhibition of DNA and histone methyltransferases increases viral mimicry in ovarian cancer cells. *Cancer Res* 78: 5754 – 5766

Lock FE, Rebollo R, Miceli-Royer K, Gagnier L, Kuah S, Babaian A, Sistiaga-Poveda M, Lai CB, Nemirovsky O, Serrano I *et al* (2014) Distinct isoform of FABP7 revealed by screening for retroelement-activated genes in diffuse large B-cell lymphoma. *Proc Natl Acad Sci USA* 111: E3534 – E3543

Lun ATL, Smyth GK (2016a) From reads to regions: a Bioconductor workflow to detect differential binding in ChIP-seq data. *F1000Res* 4: 1080

Lun ATL, Smyth GK (2016b) csaw: a Bioconductor package for differential binding analysis of ChIP-seq data using sliding windows. *Nucleic Acids Res* 44: e45

Margueron R, Li G, Sarma K, Blais A, Zavadil J, Woodcock CL, Dynlacht BD, Reinberg D (2008) Ezh1 and Ezh2 maintain repressive chromatin through different mechanisms. *Mol Cell* 32: 503 – 518

Martens JHA, O'Sullivan RJ, Braunschweig U, Opravil S, Radolf M, Steinlein P, Jenuwein T (2005) The profile of repeat-associated histone lysine methylation states in the mouse epigenome. *EMBO J* 24: 800 – 812

McCabe MT, Ott HM, Ganji G, Korenchuk S, Thompson C, Van Aller GS, Liu Y, Graves AP, Iii ADP, Diaz E *et al* (2012) EZH2 inhibition as a therapeutic strategy for lymphoma with EZH2-activating mutations. *Nature* 492: 108 – 112

Mootha VK, Lindgren CM, Eriksson K-F, Subramanian A, Sihag S, Lehar J, Puigserver P, Carlsson E, Ridderstråle M, Laurila E *et al* (2003) PGC-1α-responsive genes involved in oxidative phosphorylation are coordinately downregulated in human diabetes. *Nat Genet* 34: 267 – 273

Morel KL, Sheahan AV, Burkhart DL, Baca SC, Boufaied N, Liu Y, Qiu X, Cañadas I, Roehle K, Heckler M *et al* (2021) EZH2 inhibition activates a dsRNA-STING-interferon stress axis that potentiates response to PD-1 checkpoint blockade in prostate cancer. *Nat Cancer* 2: 444 – 456

Morschhauser F, Tilly H, Chaidos A, McKay P, Phillips T, Assouline S, Batlevi CL, Campbell P, Ribrag V, Damaj GL *et al* (2020) Tazemetostat for patients with relapsed or refractory follicular lymphoma: an open-label, single-arm, multicentre, phase 2 trial. *Lancet Oncol* 21: 1433 – 1442

Müller J, Hart CM, Francis NJ, Vargas ML, Sengupta A, Wild B, Miller EL, O'Connor MB, Kingston RE, Simon JA (2002) Histone methyltransferase activity of a Drosophila Polycomb group repressor complex. *Cell* 111: 197 – 208

Müller F, Scherer M, Assenov Y, Lutsik P, Walter J, Lengauer T, Bock C (2019) RnBeads 2.0: comprehensive analysis of DNA methylation data. *Genome Biol* 20: 55

Nakayama T, Hieshima K, Nagakubo D, Sato E, Nakayama M, Kawa K, Yoshie O (2004) Selective induction of Th2-attracting chemokines CCL17 and CCL22 in human B cells by latent membrane protein 1 of Epstein-Barr virus. *J Virol* 78: 1665 – 1674

Panning B, Smiley JR (1989) Regulation of cellular genes transduced by herpes simplex virus. *J Virol* 63: 1929 – 1937

Panning B, Smiley JR (1993) Activation of RNA polymerase III transcription of human Alu repetitive elements by adenovirus type 5: requirement for the E1b 58-kilodalton protein and the products of E4 open reading frames 3 and 6. *Mol Cell Biol* 13: 3231 – 3244

Quinlan AR, Hall IM (2010) BEDTools: a flexible suite of utilities for comparing genomic features. *Bioinformatics* 26: 841 – 842

Ramírez F, Ryan DP, Grüning B, Bhardwaj V, Kilpert F, Richter AS, Heyne S, Dündar F, Manke T (2016) deepTools2: a next generation web server for deep-sequencing data analysis. *Nucleic Acids Res* 44: W160 – W165

Rickinson AB, Moss DJ (1997) Human cytotoxic T lymphocyte responses to Epstein-Barr virus infection. *Annu Rev Immunol* 15: 405 – 431

Robinson MD, McCarthy DJ, Smyth GK (2010) edgeR: a Bioconductor package for differential expression analysis of digital gene expression data. *Bioinformatics* 26: 139 – 140

Robinson JT, Thorvaldsdóttir H, Winckler W, Guttman M, Lander ES, Getz G, Mesirov JP (2011) Integrative genomics viewer. *Nat Biotechnol* 29: 24 – 26

Rodriguez-Martin B, Alvarez EG, Baez-Ortega A, Zamora J, Supek F, Demeulemeester J, Santamarina M, Ju YS, Temes J, Garcia-Souto D *et al* (2020) Pan-cancer analysis of whole genomes identifies driver rearrangements promoted by LINE-1 retrotransposition. *Nat Genet* 52: 306 – 319

Rohraff DM, He Y, Farkash EA, Schonfeld M, Tsou P-S, Sawalha AH (2019) Inhibition of EZH2 ameliorates lupus-like disease in MRL/lpr mice. *Arthritis Rheumatol* 71: 1681 – 1690

Roulois D, Loo Yau H, Singhania R, Wang Y, Danesh A, Shen SY, Han H, Liang G, Jones PA, Pugh TJ *et al* (2015) DNA-demethylating agents target colorectal cancer cells by inducing viral mimicry by endogenous transcripts. *Cell* 162: 961 – 973

Schmidt A, Rothenfusser S, Hopfner K-P (2012) Sensing of viral nucleic acids by RIG-I: from translocation to translation. *Eur J Cell Biol* 91: 78 – 85

Schuettengruber B, Chourrout D, Vervoort M, Leblanc B, Cavalli G (2007) Genome regulation by polycomb and trithorax proteins. *Cell* 128: 735 – 745

Smith C, Beagley L, Khanna R (2009) Acquisition of polyfunctionality by Epstein-Barr virus-specific $CD8^+$ T cells correlates with increased resistance to galectin-1-mediated suppression. *J Virol* 83: 6192 – 6198

Souroullas GP, Jeck WR, Parker JS, Simon JM, Liu J-Y, Paulk J, Xiong J, Clark KS, Fedoriw Y, Qi J *et al* (2016) An oncogenic Ezh2 mutation induces tumors through global redistribution of histone 3 lysine 27 trimethylation. *Nat Med* 22: 632 – 640

Stetson DB, Medzhitov R (2006) Recognition of cytosolic DNA activates an IRF3-dependent innate immune response. *Immunity* 24: 93 – 103

Su IH, Basavaraj A, Krutchinsky AN, Hobert O, Ullrich A, Chait BT, Tarakhovsky A (2003) Ezh2 controls B cell development through histone H3 methylation and Igh rearrangement. *Nat Immunol* 4: 124 – 131

Subramanian A, Tamayo P, Mootha VK, Mukherjee S, Ebert BL, Gillette MA, Paulovich A, Pomeroy SL, Golub TR, Lander ES *et al* (2005) Gene set enrichment analysis: a knowledge-based approach for interpreting genome-wide expression profiles. *Proc Natl Acad Sci USA* 102: 15545 – 15550

Tamburri S, Lavarone E, Fernández-Pérez D, Conway E, Zanotti M, Manganaro D, Pasini D (2020) Histone H2AK119 mono-ubiquitination is essential for polycomb-mediated transcriptional repression. *Mol Cell* 77: 840 – 856

Teissandier A, Servant N, Barillot E, Bourc'his D (2019) Tools and best practices for retrotransposon analysis using high-throughput sequencing data. *Mob DNA* 10: 52

U.S. Food and Drug Administration (2020) *FDA approves first treatment option specifically for patients with epithelioid sarcoma, a rare soft tissue cancer*. Silver Spring, MD: FDA

Varambally S, Dhanasekaran SM, Zhou M, Barrette TR, Kumar-Sinha C, Sanda MG, Ghosh D, Pienta KJ, Sewalt RGAB, Otte AP *et al* (2002) The polycomb group protein EZH2 is involved in progression of prostate cancer. *Nature* 419: 624 – 629

Velichutina I, Shaknovich R, Geng H, Johnson NA, Gascoyne RD, Melnick AM, Elemento O (2010) EZH2-mediated epigenetic silencing in germinal center B cells contributes to proliferation and lymphomagenesis. *Blood* 116: 5247 – 5255

Wang H, Wang L, Erdjument-Bromage H, Vidal M, Tempst P, Jones RS, Zhang Y (2004) Role of histone H2A ubiquitination in Polycomb silencing. *Nature* 431: 873 – 878

Wang H, Yang H, Shivalila CS, Dawlaty MM, Cheng AW, Zhang F, Jaenisch R (2013) One-step generation of mice carrying mutations in multiple genes by CRISPR/Cas-mediated genome engineering. *Cell* 153: 910 – 918

Wang C, Li D, Zhang L, Jiang S, Liang J, Narita Y, Hou I, Zhong Q, Zheng Z, Xiao H *et al* (2019a) RNA sequencing analyses of gene expression during Epstein-Barr virus infection of primary B lymphocytes. *J Virol* 93: e00226-19

Wang C, Li D, Zhang L, Jiang S, Liang J, Narita Y, Hou I, Zhong Q, Zheng Z, Xiao H *et al* (2019b) Gene Expression Omnibus GSE125974 (https://www.ncbi.nlm.nih.gov/geo/query/acc.cgi?acc=GSE125974). [DATASET]

Wassef M, Rodilla V, Teissandier A, Zeitouni B, Gruel N, Sadacca B, Irondelle M, Charruel M, Ducos B, Michaud A *et al* (2015) Impaired PRC2 activity promotes transcriptional instability and favors breast tumorigenesis. *Genes Dev* 29: 2547 – 2562

Williams WP, Tamburic L, Astell CR (2004) Increased levels of B1 and B2 SINE transcripts in mouse fibroblast cells due to minute virus of mice infection. *Virology* 327: 233 – 241

Wu L, Jiang X, Qi C, Zhang C, Qu B, Shen N (2021) EZH2 inhibition interferes with the activation of type I interferon signaling pathway and ameliorates lupus nephritis in NZB/NZW F1 mice. *Front Immunol* 12: 653989

Yap DB, Chu J, Berg T, Schapira M, Cheng S-WG, Moradian A, Morin RD, Mungall AJ, Meissner B, Boyle M *et al* (2011) Somatic mutations at EZH2 Y641 act dominantly through a mechanism of selectively altered PRC2 catalytic activity, to increase H3K27 trimethylation. *Blood* 117: 2451 – 2459

Yin J, Leavenworth JW, Li Y, Luo Q, Xie H, Liu X, Huang S, Yan H, Fu Z, Zhang LY *et al* (2015) Ezh2 regulates differentiation and function of natural killer cells through histone methyltransferase activity. *Proc Natl Acad Sci USA* 112: 15988 – 15993

Yu G, Wang L-G, He Q-Y (2015) ChIPseeker: an R/Bioconductor package for ChIP peak annotation, comparison and visualization. *Bioinformatics* 31: 2382 – 2383

Zhang Y, Liu T, Meyer CA, Eeckhoute J, Johnson DS, Bernstein BE, Nusbaum C, Myers RM, Brown M, Li W *et al* (2008) Model-based analysis of ChIP-Seq (MACS). *Genome Biol* 9: R137

Zhang Y, Ma Z, Wang Y, Boyer J, Ni G, Cheng L, Su S, Zhang Z, Zhu Z, Qian J *et al* (2020) Streptavidin promotes DNA binding and activation of cGAS to enhance innate immunity. *iScience* 23: 101463

Zhao Y, Ding L, Wang D, Ye Z, He Y, Ma L, Zhu R, Pan Y, Wu Q, Pang K *et al* (2019) EZH2 cooperates with gain-of-function p53 mutants to promote cancer growth and metastasis. *EMBO J* 38: e99599